Title: Pickering stabilization of a dynamic intracellular emulsion

Authors: Andrew W. Folkmann[1†], Andrea Putnam[1†], Chiu Fan Lee[2], and Geraldine Seydoux[1*]

Affiliations:

[1]HHMI and Department of Molecular Biology and Genetics, Johns Hopkins University, Baltimore 21205 USA.

[2]Department of Bioengineering, Imperial College London, London SW7 2AZ, United Kingdom.

*Correspondence to: gseydoux@jhmi.edu

† These authors contributed equally to this work.

Abstract:

Biomolecular condensates are cellular compartments that can form by phase separation in the absence of limiting membranes. Studying the P granules of *C. elegans*, we find that condensate dynamics are regulated by protein clusters that adsorb to the condensate interface. Using *in vitro* reconstitution, live observations and theory, we demonstrate that localized assembly of P granules is controlled by MEG-3, an intrinsically disordered protein that forms low dynamic assemblies on P granules. Following classic Pickering emulsion theory, MEG-3 clusters lower surface tension and slow down coarsening. During zygote polarization, MEG-3 recruits DYRK/MBK-2 kinase to accelerate spatially-regulated growth of the P granule emulsion. By tuning condensate-cytoplasm exchange, interfacial clusters regulate the structural integrity of biomolecular condensates, reminiscent of the role of lipid bilayers in membrane-bound organelles.

One Sentence Summary:

Biomolecular condensates are stabilized by interfacial nanoscale protein clusters.

Main Text:

Introduction

Liquid-liquid phase separation (LLPS) has emerged as a new principle for cellular organization (*1*). Phase separation of proteins, frequently with RNA, can create dense condensates visible by microscopy as micron-scale assemblies containing dozens or more protein and RNA species. Condensates have been reconstituted *in vitro* using purified proteins that interact using multivalent, low-affinity binding sites to generate large, interconnected networks. Some proteins form condensates that exhibit fast internal dynamics and rapid exchange with the dilute phase on a time scale of seconds or minutes (*1*). Other proteins form more viscous condensates with slower internal and exchange dynamics, in some cases becoming glass-like with time (*2*, *3*). All condensate systems (emulsions) are predicted to evolve (coarsen) towards a single-condensate equilibrium at a rate that correlates positively with their internal and exchange dynamics (*4–7*) (*8*) (Supplementary text). Like condensates assembled *in vitro*, condensates in cells exhibit a range of dynamic behaviors, but these do not always fit theoretical predictions (*9*, *10*). For example, some condensates exhibit little coarsening over hour time scales, yet maintain low viscosity, fast exchange dynamics and dissolve within minutes in response to changes in the cellular environment (*11*). Several hypotheses have been put forward to explain the lack of coarsening of cellular condensates with fast internal dynamics, including physical barriers that keep condensates away from each other (*5*, *12*, *13*), active mechanisms that continuously regenerate small condensates (*14*), and chemical reactions and protein gradients that suppress Ostwald ripening (*15–18*) (see Supplemental Text). In this study, we investigate the mechanisms that control the coarsening and dynamics of P granules, condensates in the *C. elegans* germline. We find that P granule coarsening is controlled by nanoscale protein clusters that adsorb to the condensate interface, a phenomenon first described by Ramsden (1904) and Pickering (1907) for inorganic emulsions (*19*, *20*).

P granules were the first cellular condensates proposed to form by LLPS (*21*). At the core of P granules is a liquid-like phase assembled by PGL proteins (*21–23*). During most of the *C. elegans* life cycle, PGL condensates associate stably with the cytoplasmic face of nuclei (*24*). During the oocyte-to-zygote transition, PGL condensates redistribute to the cytoplasm and undergo two rapid cycles of dissolution and condensation. The first cycle occurs during oocyte maturation when most PGL condensates dissolve before reassembling after fertilization in the zygote. The second cycle occurs during zygote polarization where PGL condensates dissolve in anterior cytoplasm and assemble in posterior cytoplasm. Both cycles are completed within minutes without significant coarsening. Factors that regulate P granule dynamics during oocyte maturation have not yet been identified. Factors that regulate dynamics during polarization include MEX-5, an RNA-binding protein, MEG-3 and MEG-4, two paralogous intrinsically disordered proteins, and MBK-2, a DYRK family kinase that interacts physically and genetically with MEG-3 (*22*, *25*, *26*). During polarization, MEX-5 becomes enriched in the anterior cytoplasm where it promotes P granule dissolution, possibly by competing with P granule proteins for RNA (*22*, *27*). In zygotes lacking *mbk-2* or *meg-3 meg-4* activity, P granules do not dissolve in the anterior cytoplasm, despite a normal MEX-5 gradient (*28*). In this study, we investigate how the MEGs and MBK-2 collaborate with MEX-5 to regulate P granule dynamics.

MEG-3 forms low-dynamic clusters that adsorb to the PGL-3 interface

MEG-3 has been reported to form assemblies on the surface of PGL-3 condensates in newly fertilized zygotes (*28*, *29*) and in MEG-3/PGL-3 co-condensates reconstituted *in vitro* (*29*). Super resolution 3D confocal microscopy (see Methods) confirmed that MEG-3 forms diffraction-limited clusters (<160 nm) at the PGL-3 interface *in vivo* and *in vitro* (Fig. 1A , and fig. S1). Consistent with MEG-3 clusters adsorbing to the interface, MEG-3 modifies the wetting behavior of PGL-3 condensates assembled *in vitro*, reducing the extent to which PGL-3 droplets wet the surface of untreated glass slides (Fig. 1B and C).

MEG-3 clusters are resistant to dilution, high temperature, and salt treatment; in contrast,PGL-3 condensates readily dissolve in dilute conditions and at elevated temperatures (*29*). MEG-3 condensates exchange more slowly than PGL-3 condensates as measured by FRAP *in vitro* and *in vivo* (*29*). Using a single-molecule method adapted from Wu et al., 2019 (*30*), we measured the dynamics of MEG-3 and PGL-3 molecules in P granules *in vivo* (Fig. 1D to F, and movies S1 and S2). Most PGL-3 molecules exhibited short-lived trajectories in P granules with an average apparent diffusion coefficient of D_c = 0.056 μm^2/s (Fig. 1E and F). In contrast, all MEG-3 molecules exhibited restricted long-lived trajectories with an average apparent diffusion coefficient of Dc = 0.0018 μm^2/s (Fig. 1E and F) In 3/3 cases where we captured the trajectories of three labeled MEG-3 molecules in the same P granule, their relative position remained fixed over time (Fig. 1D, and movie S2). Together these observations confirm that PGL-3 molecules exist primarily in a dynamic liquid-like phase (albeit highly viscous), whereas MEG-3 molecules experience much slower dynamics resembling solid clusters within our experimental time scales.

MEG-3 reduces the surface tension of PGL-3 condensates without changing viscosity

Solid particulates that adsorb to liquid surfaces reduce surface tension without affecting internal dynamics (viscosity (*31*)). Previous studies have shown that PGL-3 condensates are "aging Maxwell fluids" whose viscosity increases over days, eventually adopting glass-like properties (see Supplemental Text, (*2*, *32*)). To approximate the time scales experienced by PGL-3 condensates during the oocyte-to-embryo transition, we examined PGL-3 condensates within the first three hours of assembly for all *in vitro* studies. To probe internal dynamics, we measured the movement of fluorescent beads embedded in PGL-3 condensates with and without MEG-3 (fig. S2A and B, and movie S3). Fitting bead mean squared displacement to $4Dt^{\alpha}$, we calculated a diffusion coefficient D and diffusive exponent α. We observed an $\alpha \approx 1$ for PGL-3, consistent with newly formed PGL-3 condensates behaving as viscous liquids (fig. S2C). Using the Stokes–Einstein relation, we calculated a viscosity of η = 5.4 Pa·s in the range estimated previously for PGL-3 condensates *in vivo* and *in vitro* (fig. S2C)(*2*, *21*). Addition of MEG-3 had no

significant effect on PGL-3 viscosity (η = 5.6 Pa·s) (fig. S2B to D, and movie S3), as expected for a surface agent that, on its own, does not affect internal dynamics.

To measure PGL-3 surface tension, we examined the coalescence behavior of PGL-3 droplets (Fig. 2A). Relaxation time of coalescing condensates can be expressed by $\tau \approx \ell(\eta/\gamma)$, where ℓ is the geometric mean of the diameters of the droplets at the onset of fusion, η is the viscosity of the droplets, γ is the surface tension, and η/γ is the inverse capillary velocity. PGL-3 condensates coalesce with a linear relationship over a range of condensate sizes yielding an inverse capillary velocity of 0.25 s/μm and surface tension of 19.4 μN/m (Fig. 2B, and movie S4), comparable to previous estimates for P granules *in vivo* (*21*). Addition of MEG-3 significantly slowed coalescence of PGL-3 droplets, yielding an inverse capillary velocity of 1.2 s/μm and a surface tension of 4.7 μN/m (500 nM MEG-3, Fig. 2B, and movie S5).

In addition to modulating surface tension, Pickering agents can also inhibit coalescence by steric hindrance and slow rearrangement at the condensate interface (*33*). We observed examples of MEG-3-coated PGL-3 droplets that did not relax to a sphere or remained in contact without fusing during imaging (movie S6 and S7). Higher concentrations of MEG-3 (1 μm) increased surface coverage and caused PGL-3 droplets to flocculate without fusing (fig. S2E). We conclude that, as expected for a Pickering agent, MEG-3 clusters lower the surface tension of PGL-3 condensates and also forms a physical barrier to coalescence.

MEG-3 prevents coarsening of the PGL-3 emulsion without eliminating surface exchange

To determine whether MEG-3 stabilizes the PGL-3 emulsion against coarsening, we examined the evolution of a newly assembled PGL-3 emulsion overtime. Over the course of 180 minutes, the PGL-3 emulsion coarsens significantly: droplets increased in size on average and decreased in number without a change in the total volume of PGL-3 in droplets (Fig. 2C and D, and fig. S2F to H). Addition of MEG-3 reduced coarsening, stabilizing droplet size and number over the 180 minutes of the experiment (Fig. 2C

and E, and fig. S2F to H). MEG-3 concentrations constrained the size of PGL-3 droplets in a dose-dependent manner (fig. S2I to M).

MEG-3 does not affect the internal dynamics of PGL-3 condensates as measured by FRAP (*29*). To examine whether MEG-3 prevents exchange of PGL-3 molecules at the interface, we used PGL-3 preparations trace-labeled with different fluorophores and examined mixing kinetics. Unlike MEG-3 clusters, which do not mix post-assembly, PGL-3 condensates continue to exchange post-assembly (fig. S3A to C). Addition of soluble PGL-3 to a preformed emulsion leads to the formation of new condensates that over the course of an hour completely mix with the old condensates (fig. S3D to F). Addition of MEG-3 prevented coarsening but did not affect the rate of new and old PGL-3 mixing (fig. S3D to F). We conclude that MEG-3 clusters stabilize the PGL-3 emulsion by lowering surface tension without completely blocking surface exchange, as described for other Pickering agents (*34*).

MEG-3 stabilizes PGL-3 condensates against DYRK3-accelerated coarsening

The relative high viscosity of the PGL-3 emulsion is consistent with the apparent stability of P granules during most of germline development and suggests that active processes must operate to dissolve P granules during oocyte maturation and polarization. MBK-2 kinase is required for P granule dissolution during polarization and its mammalian homolog DYRK3 has been implicated in the dissolution of condensates in mammalian cells (*28*, *35*, *36*). We found that recombinant DYRK3 phosphorylates PGL-3 efficiently *in vitro* (fig. S4A). Addition of DYRK3 and ATP to pre-assembled PGL-3 condensates (2.5 μM) led to their complete dissolution over 60 minutes (Fig. 3A and B). The effect did not depend on the hydrotrope properties of ATP (*37*) as dissolution was not observed in the presence of GTP (Fig. 3A and B). Sedimentation experiments confirmed that phosphorylation by DYRK3 increases the fraction of PGL-3 in the soluble pool (fig. S4B). At a higher concentration of PGL-3 (5 μM), condensates could be maintained in the presence of DYRK3 (Fig. 3C). We used these supersaturated conditions to conduct microrheology experiments on PGL-3 droplets treated with DYRK3 (Fig. 3D, and movie S8). We found

that DYRK3 significantly decreases the viscosity of PGL-3 droplets (Fig. 3D). Consistent with accelerated internal dynamics, DYRK3-treated PGL-3 condensates also coarsened rapidly (Fig. 3C, and E). Addition of MEG-3 did not interfere with PGL-3 phosphorylation but led to a ~3 fold-increase in the frequency of small PGL-3 droplets (Fig. 3C and E , and fig. S4D). The small droplets were covered with MEG-3 and remained stable for 120 minutes, even in the presence of much larger condensates (Fig. S4E to G). These observations indicate that MEG-3 stabilizes the PGL-3 emulsion against coarsening, even under conditions where PGL-3 dynamics have been accelerated by phosphorylation.

MEG-3/4 stabilize P granules against coarsening during the oocyte-to-zygote transition

To examine the impact of MEG-3 on P granule dynamics *in vivo*, we used quantitative live-cell imaging to measure the number and size of PGL-3 condensates in wild-type and *meg-3 meg-4* mutants. We began by imaging eggs *in utero* as they progress through oocyte maturation and fertilization (Fig. 4A and B). We found that the volume of PGL-3 in condensates decreased 10-fold during oocyte maturation and remained low in newly fertilized zygotes as they complete the meiotic divisions (Fig. 4C to F, and fig. S5A). Total PGL-3 levels did not change during this period (fig. S5B) consistent with a transient increase in PGL-3 solubility. We observed the same decrease in PGL-3 condensate volume in wild-type and *meg-3 meg-4* oocytes, indicating that the increase in PGL-3 solubility during the oocyte-to-zygote transition is not dependent on *meg-3 meg-4* (Fig. 4C to F, and fig. S5A and B). The size distribution of PGL-3 condensates post-dissolution, however, was different in the two genotypes. The PGL-3 emulsion coarsened rapidly in *meg-3 meg-4* zygotes with fewer larger condensates dominating the emulsion (Fig. 4B and E). In contrast, wild-type zygotes maintained many small PGL-3 condensates, consistent with MEG-3 stabilizing the PGL-3 emulsion against coarsening (Fig. 4B and E). Zygotes in late meiosis can survive outside of the uterus allowing for the acquisition of high-resolution images *ex utero*. These images confirmed that wild-type zygotes contain dozens of <1 μm condensates not observed in *meg-3 meg-4* zygotes (Fig. 4B and F).

These observations suggest that MEG-3 functions as a Pickering agent for the PGL-3 emulsion. To examine the physical plausibility of this hypothesis, we modeled *in silico* the kinetics of an idealized PGL-3 emulsion in the presence or absence of a Pickering agent that lowers surface tension. To account for the intrinsically slow dynamics of PGL-3 condensates, we modeled PGL-3 dynamics under a "conversion-limited" scheme, where the soluble-to-condensate conversion rate of PGL-3 molecules is much slower than their diffusion-limited adsorption/desorption rate, and therefore rate limiting for condensate growth/degrowth (see Supplemental Text). To model dissolution of PGL-3 condensates during oocyte maturation, we assigned a relatively high conversion rate to PGL-3 condensates and a high critical concentration for PGL-3 phase separation since most PGL-3 condensate dissolve during this period. To model MEG-3 as a Pickering agent, we reduced the Gibbs-Thomson length (proportional to surface tension) of MEG-3-coated PGL-3 condensates by a 100-fold compared to PGL-3-only condensates. Parameter sweeps revealed that reductions in the Gibbs-Thomson length as low as two-fold, within the range observed *in vitro* (Fig. 2), were sufficient to show the same quantitative behavior (Supplemental text). We used the model to run simulations tracking the dynamics of condensates with starting sizes matching the distribution of PGL-3 condensates in oocytes post-dissolution (Fig. 4G and H). Coarsening was strikingly different in the presence or absence of the Pickering agent, with stabilization of smaller condensates requiring the Pickering agent. The simulations reproduced the increase in average condensate volume observed in *meg-3 meg-4* zygotes in comparison to wild-type zygotes (Fig. 4I and J). These results support the hypothesis that MEG-3 stabilizes the PGL-3 emulsion against an increase in PGL-3 dynamics in newly fertilized zygotes by lowering the surface tension of PGL-3 condensates.

MEG-3/4 drive asymmetric growth of the P granule emulsion during polarization

Next, we examined PGL-3 dynamics as zygotes transition from unpolarized to polarized. During this period, zygotes exit meiosis, assemble pronuclei that migrate to the center of the zygote, fuse and initiate the first mitotic division, and MEX-5 redistributes in an anterior-rich gradient (Fig. 5A). During pronuclear migration, we observed new PGL-3 condensates appearing throughout the cytoplasm in both

wild-type and *meg-3 meg-4* zygotes (Fig. 5B and C, and fig. S6A). The total volume of PGL-3 in condensates also increased (fig. S6B), without a change in total PGL-3 (fig. S6C), consistent with a return to low PGL-3 solubility in both genotypes. During this period, total condensate volume in the anterior half of the zygote decreased steadily eventually reaching zero, while total condensate volume in the posterior increased (Fig. 5D). Remarkably, in *meg-3 meg-4* zygotes, we also observed a decrease and increase in total condensate volume in the anterior and posterior, respectively, but the amplitude of the change was greatly reduced (Fig. 5E). By mitosis, in wild-type, all PGL-3 condensates were restricted to the posterior cytoplasm; in contrast, in *meg-3 meg-4* zygotes, PGL-3 condensates remained stable throughout the cytoplasm through the first cell division (Fig. 5A to E), suggesting that in *meg-3 meg-4* mutants, the PGL-3 emulsion does not respond efficiently to the MEX-5-driven solubility gradient.

To examine condensate dynamics directly, we tracked individual PGL-3 condensates in live zygotes from pronuclear formation to pronuclear meeting (Fig. 5F to I, and movie S9). These observations confirmed that, in *meg-3 meg-4* zygotes, condensates experience very slow growth/dissolution rates during polarization, with a slight bias for decay in the anterior ($k^{A,avg}$ -0.19 nm/s, $k^{P,avg}$ = 0.06 nm/s, Fig. 5G and I). Growth/decay rates were more than 5-fold faster in wild-type zygotes with a clear bias for dissolution in the anterior and condensation in the posterior ($k^{A,avg}$ -1.18 µm/s, $k^{P,avg}$ = 0.50 µm/s, Fig. 5F and H). These findings suggest that, unlike in oocytes where PGL-3 dissolution occurs independently of *meg-3* and *meg-4*, during polarization *meg-3* and *meg-4* are required to accelerate PGL-3 condensate dynamics.

In addition to *meg-3* and *meg-4*, P granule dissolution during polarization requires the DYRK kinase MBK-2 (*38*, *39*). Genetic epistasis experiments have shown that MBK-2's dissolution activity is dependent on *meg-3* and *meg-4* (*28*) (Supplementary text). Consistent with these observations, using an epitope tagged allele of endogenous MBK-2, we found that MBK-2 is recruited to PGL-3 condensates during polarization and this recruitment is diminished in *meg-3 meg-4* mutant embryos (Fig. 5J and K). MEG-3 and MBK-2 levels varied more than five-fold among PGL-3 condensates (fig. S6D to G). Condensate growth rates during polarization were also heterogeneous in a manner that did not correlate

with initial condensate size (Fig. 5F and G). Together, these observations suggest that heterogeneous recruitment of MEG-3/MBK-2 variably accelerates PGL-3 condensate dynamics during polarization.

Based on these findings, we built on our theoretical model of the PGL-3 emulsion adding three new features specific to polarization: 1) variable soluble-to-condensate conversion rates for PGL-3 condensates to reflect heterogeneous fluidization by MEG-3/MBK-2, 2) higher solubility for PGL-3 in anterior cytoplasm to reflect the influence of the MEX-5 gradient, and 3) lower Gibbs-Thomson lengths for posterior condensates to reflect sustained coverage of posterior condensates by MEG-3 ("asymmetric Pickering agent"). Parameters were benchmarked to allow for complete dissolution of anterior granules in ~6 minutes as observed *in vivo*. We used the model to run simulations tracking the growth and decay of condensates matching the size distribution of PGL-3 condensates *in vivo* pre-polarization. The simulations faithfully recapitulated the coarsening-free dissolution of anterior condensates and growth of posterior condensates observed in wild-type zygotes (Fig. 5L, and movie S10). Simulations mimicking conditions in *meg-3 meg-4* mutants reproduced the slow dynamics observed in those mutants (Fig. 5M, and movie S10). The simulations also reproduced the rapid increase in PGL-3 condensate volume (fig. S6H) that is observed during mitosis in wild-type but not *meg-3 meg-4* zygotes (fig. S5A, and S6B). The rapid rise is a consequence of the faster approach to equilibrium in the supersaturated environment of the posterior cytoplasm by PGL-3 condensates with accelerated dynamics driven by MEG-3/MBK-2.

To test the importance of each feature in the model, we reran the wild-type simulations changing one model feature at a time. Simulations where condensates were assigned uniformly low conversion rates yielded decay rates that were too slow to clear anterior granules under the *in vivo* time constraints (fig. S6I, and movie S10). Simulations with low PGL-3 solubility across the cytoplasm led to coarsening of anterior condensates (fig. S6J, and movie S10). Simulations lacking the Pickering agent led to coarsening of posterior condensates (fig. S6K, and movie S10). Together with the *in vitro* and *in vivo* findings, the theory supports a model where MEG-3 facilitates P granules polarization in response to the MEX-5-induced saturation gradient by accelerating PGL-3 conversion dynamics (via recruitment of MBK-2) and by functioning as a Pickering agent to lower surface tension on posterior condensates thus

preventing coarsening during periods of fast PGL dynamics (Fig. 6; Supplemental Text for a full discussion of theoretical considerations).

Discussion

Since their description by Ramsden and Pickering in the early 1900s (*19*, *20*), Pickering agents have been used widely to stabilize emulsions in the pharmaceutical, energy and food industries (*40–42*). Unlike surfactants (amphiphilic molecules that insert at interfaces), Pickering agents are nanoscale solid particulates that adsorb to interfaces upon partial wetting by both phases. Adsorption is energetically favored and balances the drive to reduce interfacial area, stabilizing the emulsion against coarsening (*43*). Many types of solid particulates have been shown to function as Pickering agents, from silica to denatured proteins (*44*). The first described intrinsically disordered protein, casein, functions as a natural Pickering agent in homogenized milk (*45*). To our knowledge, the intrinsically disordered protein MEG-3 is the first characterized example of an *intracellular* Pickering agent and we speculate that other self-assembling biopolymers will exhibit similar properties. In somatic cells, PGL droplets are covered by EPG-2 clusters that may function like MEG-3 to regulate the size and dynamics of PGL droplets in preparation for autophagy (*46*). Artificial protein-RNA assemblies that adsorb to the surface of stress granules have been reported to influence their size and coalescence (*47*). mRNAs that accumulate on the surface of protein condensates could also serve as stabilizing agents (*48*, *49*). Given the rich diversity of biopolymers in cells, it is tempting to speculate that biopolymers acting as Pickering agents will prove a general organizing principle for biomolecular condensates. By interacting with enzymes like the DYRK kinase MBK-2, biological Pickering agents also regulate interfacial exchange to control the influx and efflux of molecules in and out of condensates in response to environmental changes. In this respect, surface-adsorbed biopolymers fulfill a boundary function for biomolecular condensates, reminiscent of the role of lipid bilayers and associated machineries (e.g. channels) in membrane-bound organelles. In fact, it has been speculated that lipid membranes arose from liposomes that functioned as Pickering stabilizers for aqueous emulsions (*50*).

References and Notes:

1. A. A. Hyman, C. A. Weber, F. Jülicher, Liquid-Liquid Phase Separation in Biology. *Annu. Rev. Cell Dev. Biol.* **30**, 39–58 (2014).

2. L. Jawerth, E. Fischer-Friedrich, S. Saha, J. Wang, T. Franzmann, X. Zhang, J. Sachweh, M. Ruer, M. Ijavi, S. Saha, J. Mahamid, A. A. Hyman, F. Jülicher, Protein condensates as aging Maxwell fluids. *Science*. **370**, 1317–1323 (2020).

3. S. Boeynaems, S. Alberti, N. L. Fawzi, T. Mittag, M. Polymenidou, F. Rousseau, J. Schymkowitz, J. Shorter, B. Wolozin, L. Van Den Bosch, P. Tompa, M. Fuxreiter, Protein Phase Separation: A New Phase in Cell Biology. *Trends in Cell Biology*. **28**, 420–435 (2018).

4. E. S. Freeman Rosenzweig, B. Xu, L. K. Cuellar, A. Martinez-Sanchez, M. Schaffer, M. Strauss, H. N. Cartwright, P. Ronceray, J. M. Plitzko, F. Förster, N. S. Wingreen, B. D. Engel, L. C. M. Mackinder, M. C. Jonikas, The Eukaryotic CO2-Concentrating Organelle is Liquid-Like and Exhibits Dynamic Reorganization. *Cell*. **171**, 148-162.e19 (2017).

5. M. Feric, C. P. Brangwynne, A nuclear F-actin scaffold stabilizes ribonucleoprotein droplets against gravity in large cells. *Nature Cell Biology*. **15**, 1253–1259 (2013).

6. J. Berry, S. C. Weber, N. Vaidya, M. Haataja, C. P. Brangwynne, RNA transcription modulates phase transition-driven nuclear body assembly. *Proc Natl Acad Sci USA*. **112**, E5237–E5245 (2015).

7. S. Elbaum-Garfinkle, Y. Kim, K. Szczepaniak, C. C.-H. Chen, C. R. Eckmann, S. Myong, C. P. Brangwynne, The disordered P granule protein LAF-1 drives phase separation into droplets with tunable viscosity and dynamics. *Proc Natl Acad Sci USA*. **112**, 7189–7194 (2015).

8. S. Ranganathan, E. I. Shakhnovich, Dynamic metastable long-living droplets formed by sticker-spacer proteins. *eLife*. **9**, e56159 (2020).

9. J. Berry, C. P. Brangwynne, M. Haataja, Physical principles of intracellular organization via active and passive phase transitions. *Rep. Prog. Phys.* **81**, 046601 (2018).

10. D. T. McSwiggen, M. Mir, X. Darzacq, R. Tjian, Evaluating phase separation in live cells: diagnosis, caveats, and functional consequences. *Genes Dev.* **33**, 1619–1634 (2019).

11. J. R. Wheeler, T. Matheny, S. Jain, R. Abrisch, R. Parker, Distinct stages in stress granule assembly and disassembly. *eLife*. **5**, doi:10.7554/eLife.18413.

12. J. E. Lee, P. I. Cathey, H. Wu, R. Parker, G. K. Voeltz, Endoplasmic reticulum contact sites regulate the dynamics of membraneless organelles. *Science*. **367** (2020), doi:10.1126/science.aay7108.

13. D. S. W. Lee, N. S. Wingreen, C. P. Brangwynne, Chromatin mechanics dictates subdiffusion and coarsening dynamics of embedded condensates. *Nature Physics*. **17**, 531–538 (2021).

14. C. F. Lee, C. P. Brangwynne, J. Gharakhani, A. A. Hyman, F. Jülicher, Spatial organization of the cell cytoplasm by position-dependent phase separation. *Phys Rev Lett*. **111**, 088101 (2013).

15. C. A. Weber, C. F. Lee, F. Jülicher, Droplet ripening in concentration gradients. *New Journal of Physics*. **19**, 053021 (2017).

16. D. Zwicker, A. A. Hyman, F. Jülicher, Suppression of Ostwald ripening in active emulsions. *Phys. Rev. E*. **92**, 012317 (2015).

17. P. C. Bressloff, Active suppression of Ostwald ripening: Beyond mean-field theory. *Phys. Rev. E*. **101**, 042804 (2020).

18. J. D. Wurtz, C. F. Lee, Chemical-Reaction-Controlled Phase Separated Drops: Formation, Size Selection, and Coarsening. *Phys. Rev. Lett.* **120**, 078102 (2018).

19. W. Ramsden, F. Gotch, Separation of solids in the surface-layers of solutions and 'suspensions' (observations on surface-membranes, bubbles, emulsions, and mechanical coagulation).—Preliminary account. *Proceedings of the Royal Society of London*. **72**, 156–164 (1904).

20. S. U. Pickering, CXCVI.—Emulsions. *J. Chem. Soc., Trans.* **91**, 2001–2021 (1907).

21. C. P. Brangwynne, C. R. Eckmann, D. S. Courson, A. Rybarska, C. Hoege, J. Gharakhani, F. Julicher, A. A. Hyman, Germline P Granules Are Liquid Droplets That Localize by Controlled Dissolution/Condensation. *Science*. **324**, 1729–1732 (2009).

22. S. Saha, C. A. Weber, M. Nousch, O. Adame-Arana, C. Hoege, M. Y. Hein, E. Osborne-Nishimura, J. Mahamid, M. Jahnel, L. Jawerth, A. Pozniakovski, C. R. Eckmann, F. Jülicher, A. A. Hyman, Polar Positioning of Phase-Separated Liquid Compartments in Cells Regulated by an mRNA Competition Mechanism. *Cell*. **166**, 1572-1584.e16 (2016).

23. M. Hanazawa, M. Yonetani, A. Sugimoto, PGL proteins self associate and bind RNPs to mediate germ granule assembly in C. elegans. *The Journal of Cell Biology*. **192**, 929–937 (2011).

24. U. Sheth, J. Pitt, S. Dennis, J. R. Priess, Perinuclear P granules are the principal sites of mRNA export in adult C. elegans germ cells. *Development*. **137**, 1305–1314 (2010).

25. C. M. Schubert, R. Lin, C. J. de Vries, R. H. Plasterk, J. R. Priess, MEX-5 and MEX-6 function to establish soma/germline asymmetry in early C. elegans embryos. *Mol Cell*. **5**, 671–682 (2000).

26. J.-X. Chen, P. G. Cipriani, D. Mecenas, J. Polanowska, F. Piano, K. C. Gunsalus, M. Selbach, In Vivo Interaction Proteomics in Caenorhabditis elegans Embryos Provides New Insights into P Granule Dynamics. *Mol Cell Proteomics*. **15**, 1642–1657 (2016).

27. J. Smith, D. Calidas, H. Schmidt, T. Lu, D. Rasoloson, G. Seydoux, Spatial patterning of P granules by RNA-induced phase separation of the intrinsically-disordered protein MEG-3. *eLife*. **5**, e21337 (2016).

28. J. T. Wang, J. Smith, B.-C. Chen, H. Schmidt, D. Rasoloson, A. Paix, B. G. Lambrus, D. Calidas, E. Betzig, G. Seydoux, Regulation of RNA granule dynamics by phosphorylation of serine-rich, intrinsically disordered proteins in C. elegans. *eLife*. **3**, e04591 (2014).

29. A. Putnam, M. Cassani, J. Smith, G. Seydoux, A gel phase promotes condensation of liquid P granules in Caenorhabditis elegans embryos. *Nat Struct Mol Biol*. **26**, 220–226 (2019).

30. Y. Wu, B. Han, T. J. Gauvin, J. Smith, A. Singh, E. E. Griffin, Single-molecule dynamics of the P granule scaffold MEG-3 in the Caenorhabditis elegans zygote. *Mol. Biol. Cell*. **30**, 333–345 (2019).

31. *Particle-Stabilized Emulsions and Colloids* (2014; https://pubs.rsc.org/en/content/ebook/978-1-84973-881-1).

32. L. M. Jawerth, M. Ijavi, M. Ruer, S. Saha, M. Jahnel, A. A. Hyman, F. Jülicher, E. Fischer-Friedrich, Salt-Dependent Rheology and Surface Tension of Protein Condensates Using Optical Traps. *Phys. Rev. Lett.* **121**, 258101 (2018).

33. A. B. Pawar, M. Caggioni, R. Ergun, R. W. Hartel, P. T. Spicer, Arrested coalescence in Pickering emulsions. *Soft Matter*. **7**, 7710–7716 (2011).

34. C. D. Crowe, C. D. Keating, Liquid–liquid phase separation in artificial cells. *Interface Focus*. **8**, 20180032 (2018).

35. K. M. Pang, T. Ishidate, K. Nakamura, M. Shirayama, C. Trzepacz, C. M. Schubert, J. R. Priess, C. C. Mello, The minibrain kinase homolog, mbk-2, is required for spindle positioning and asymmetric cell division in early C. elegans embryos. *Dev Biol*. **265**, 127–139 (2004).

36. A. K. Rai, J.-X. Chen, M. Selbach, L. Pelkmans, Kinase-controlled phase transition of membraneless organelles in mitosis. *Nature*. **559**, 211–216 (2018).

37. A. Patel, L. Malinovska, S. Saha, J. Wang, S. Alberti, Y. Krishnan, A. A. Hyman, ATP as a biological hydrotrope. *Science*. **356**, 753–756 (2017).

38. S. Quintin, P. E. Mains, A. Zinke, A. A. Hyman, The mbk-2 kinase is required for inactivation of MEI-1/katanin in the one-cell Caenorhabditis elegans embryo. *EMBO reports*. **4**, 1175–1181 (2003).

39. J. Pellettieri, V. Reinke, S. K. Kim, G. Seydoux, Coordinate Activation of Maternal Protein Degradation during the Egg-to-Embryo Transition in C. elegans. *Developmental Cell*. **5**, 451–462 (2003).

40. C. C. Berton-Carabin, K. Schroën, Pickering Emulsions for Food Applications: Background, Trends, and Challenges. *Annual Review of Food Science and Technology*. **6**, 263–297 (2015).

41. F. Goodarzi, S. Zendehboudi, A Comprehensive Review on Emulsions and Emulsion Stability in Chemical and Energy Industries. *The Canadian Journal of Chemical Engineering*. **97**, 281–309 (2019).

42. C. Albert, M. Beladjine, N. Tsapis, E. Fattal, F. Agnely, N. Huang, Pickering emulsions: Preparation processes, key parameters governing their properties and potential for pharmaceutical applications. *Journal of Controlled Release*. **309**, 302–332 (2019).

43. D. Gonzalez Ortiz, C. Pochat-Bohatier, J. Cambedouzou, M. Bechelany, P. Miele, Current Trends in Pickering Emulsions: Particle Morphology and Applications. *Engineering*. **6**, 468–482 (2020).

44. Y. Yang, Z. Fang, X. Chen, W. Zhang, Y. Xie, Y. Chen, Z. Liu, W. Yuan, An Overview of Pickering Emulsions: Solid-Particle Materials, Classification, Morphology, and Applications. *Front. Pharmacol.* **8**, 287 (2017).

45. E. Redwan, B. Xue, H. Almehdar, V. Uversky, Disorder in Milk proteins caseins, intrinsically disordered (2015).

46. G. Zhang, Z. Wang, Z. Du, H. Zhang, mTOR Regulates Phase Separation of PGL Granules to Modulate Their Autophagic Degradation. *Cell*. **174**, 1492-1506.e22 (2018).

47. M. Garcia-Jove Navarro, S. Kashida, R. Chouaib, S. Souquere, G. Pierron, D. Weil, Z. Gueroui, RNA is a critical element for the sizing and the composition of phase-separated RNA–protein condensates. *Nature Communications*. **10**, 3230 (2019).

48. B. Hampoelz, A. Schwarz, P. Ronchi, H. Bragulat-Teixidor, C. Tischer, I. Gaspar, A. Ephrussi, Y. Schwab, M. Beck, Nuclear Pores Assemble from Nucleoporin Condensates During Oogenesis. *Cell*. **179**, 671-686.e17 (2019).

49. D. Tauber, G. Tauber, A. Khong, B. Van Treeck, J. Pelletier, R. Parker, Modulation of RNA Condensation by the DEAD-Box Protein eIF4A. *Cell*. **180**, 411-426.e16 (2020).

50. D. C. Dewey, C. A. Strulson, D. N. Cacace, P. C. Bevilacqua, C. D. Keating, Bioreactor droplets from liposome-stabilized all-aqueous emulsions. *Nature Communications*. **5**, 4670 (2014).

51. S. Brenner, The genetics of Caenorhabditis elegans. *Genetics*. **77**, 71–94 (1974).

52. A. Paix, A. Folkmann, G. Seydoux, Precision genome editing using CRISPR-Cas9 and linear repair templates in C. elegans. *Methods*. **121–122**, 86–93 (2017).

53. J. Schindelin, I. Arganda-Carreras, E. Frise, V. Kaynig, M. Longair, T. Pietzsch, S. Preibisch, C. Rueden, S. Saalfeld, B. Schmid, J.-Y. Tinevez, D. J. White, V. Hartenstein, K. Eliceiri, P. Tomancak, A. Cardona, Fiji: an open-source platform for biological-image analysis. *Nature Methods*. **9**, 676–682 (2012).

54. TNF and IL-1 exhibit distinct ubiquitin requirements for inducing NEMO–IKK supramolecular structures | Journal of Cell Biology | Rockefeller University Press, (available at https://rupress.org/jcb/article/204/2/231/37431/TNF-and-IL-1-exhibit-distinct-ubiquitin).

55. C. Y. S. Lee, A. Putnam, T. Lu, S. X. He, J. P. T. Ouyang, G. Seydoux, Recruitment of mRNAs to P granules by condensation with intrinsically-disordered proteins. *eLife*. **9**, e52896 (2020).

56. J. E. Tropea, S. Cherry, D. S. Waugh, Expression and purification of soluble His(6)-tagged TEV protease. *Methods Mol. Biol.* **498**, 297–307 (2009).

57. S. Elbaum-Garfinkle, Y. Kim, K. Szczepaniak, C. C.-H. Chen, C. R. Eckmann, S. Myong, C. P. Brangwynne, The disordered P granule protein LAF-1 drives phase separation into droplets with tunable viscosity and dynamics. *Proceedings of the National Academy of Sciences*. **112**, 7189–7194 (2015).

58. J.-Y. Tinevez, N. Perry, J. Schindelin, G. M. Hoopes, G. D. Reynolds, E. Laplantine, S. Y. Bednarek, S. L. Shorte, K. W. Eliceiri, TrackMate: An open and extensible platform for single-particle tracking. *Methods*. **115**, 80–90 (2017).

59. C. P. Brangwynne, C. R. Eckmann, D. S. Courson, A. Rybarska, C. Hoege, J. Gharakhani, F. Julicher, A. A. Hyman, Germline P Granules Are Liquid Droplets That Localize by Controlled Dissolution/Condensation. *Science*. **324**, 1729–1732 (2009).

60. K. Rhine, S. Skanchy, S. Myong, Single-molecule and ensemble methods to probe RNP nucleation and condensate properties. *Methods* (2021), doi:10.1016/j.ymeth.2021.02.012.

61. Y. Lin, D. S. W. Protter, M. K. Rosen, R. Parker, Formation and Maturation of Phase-Separated Liquid Droplets by RNA-Binding Proteins. *Molecular Cell*. **60**, 208–219 (2015).

62. A. Patel, H. O. Lee, L. Jawerth, S. Maharana, M. Jahnel, M. Y. Hein, S. Stoynov, J. Mahamid, S. Saha, T. M. Franzmann, A. Pozniakovski, I. Poser, N. Maghelli, L. A. Royer, M. Weigert, E. W. Myers, S. Grill, D. Drechsel, A. A. Hyman, S. Alberti, A Liquid-to-Solid Phase Transition of the ALS Protein FUS Accelerated by Disease Mutation. *Cell*. **162**, 1066–1077 (2015).

63. M. Rubinstein, A. N. Semenov, Dynamics of Entangled Solutions of Associating Polymers. *Macromolecules*. **34**, 1058–1068 (2001).

64. P. Taylor, Ostwald ripening in emulsions. *Advances in Colloid and Interface Science*. **75**, 107–163 (1998).

65. J. Söding, D. Zwicker, S. Sohrabi-Jahromi, M. Boehning, J. Kirschbaum, Mechanisms for Active Regulation of Biomolecular Condensates. *Trends in Cell Biology*. **30**, 4–14 (2020).

66. D. S. W. Lee, N. S. Wingreen, C. P. Brangwynne, "Chromatin Mechanics Dictates Subdiffusion and Coarsening Dynamics of Embedded Condensates" (preprint, Biophysics, 2020), , doi:10.1101/2020.06.03.128561.

67. J. D. Wurtz, C. F. Lee, Stress granule formation via ATP depletion-triggered phase separation. *New J. Phys.* **20**, 045008 (2018).

68. I. Lifshitz, V. Slyozov, The kinetics of precipitation from supersaturated solid solutions. *Journal of Physics and Chemistry of Solids*. **19**, 35–50 (1961).

69. C. A. Weber, D. Zwicker, F. Jülicher, C. F. Lee, Physics of active emulsions. *Reports on Progress in Physics*. **82**, 064601 (2019).

70. L. Jawerth, E. Fischer-Friedrich, S. Saha, J. Wang, T. Franzmann, X. Zhang, J. Sachweh, M. Ruer, M. Ijavi, S. Saha, J. Mahamid, A. A. Hyman, F. Jülicher, Protein condensates as aging Maxwell fluids. *Science*. **370**, 1317–1323 (2020).

71. S. Ranganathan, E. I. Shakhnovich, Dynamic metastable long-living droplets formed by sticker-spacer proteins. *eLife*. **9**, e56159 (2020).

72. C. F. Lee, C. P. Brangwynne, J. Gharakhani, A. A. Hyman, F. Jülicher, Spatial organization of the cell cytoplasm by position-dependent phase separation. *Physical Review Letters*. **111**, 088101 (2013).

73. J. P. T. Ouyang, A. Folkmann, L. Bernard, C.-Y. Lee, U. Seroussi, A. G. Charlesworth, J. M. Claycomb, G. Seydoux, P Granules Protect RNA Interference Genes from Silencing by piRNAs. *Developmental Cell*. **50**, 716-728.e6 (2019).

74. C. F. Lee, J. Loken, L. Jean, D. J. Vaux, Elongation dynamics of amyloid fibrils: A rugged energy landscape picture. *Phys. Rev. E*. **80**, 041906 (2009).

Acknowledgments:

We thank the Johns Hopkins Integrated Imaging center (S10OD023548) for microscopy support. We thank the Lavis lab for HaloTag Ligands JF_{549} and JF_{646}, the Griffin lab for MEG-3::Halo strain, We thank the Waugh Lav for TEV protease (pRK793, Addgene), Tony Hyman, the Baltimore Worm club and the Seydoux lab for many helpful discussions. **Funding:** This work was supported by the National Institutes of Health (GS: Grant number R37HD037047, AP: F32GM134630). GS is an investigator of the Howard Hughes Medical Institute. **Author Contributions:** A.W.F., A.P., and G.S. designed the research. A.W.F. and A.P. performed all experiments, collected, and analyzed data. C.F.L. performed the theoretical analysis. A.W.F., A.P., C.F.L., and G.S. prepared the manuscript with contributions from all authors. **Competing interests:** G.S. serves on the Scientific Advisory Board of Dewpoint Therapeutics, Inc. **Data and materials availability:** All data are available in the manuscript or the supplementary materials. Other data supporting the findings of this study are available from the corresponding author upon reasonable request.

Supplementary Materials:

Materials and Methods

Tables S1-S2

Figures S1-S9

Movies S1-S10

References (51-74)

Fig. 1. MEG-3 forms low-dynamic clusters that absorb to the surface of PGL-3 condensates.

A) Photomicrographs of a P granule *in vivo* labeled with PGL-3::mCherry and MEG-3::meGFP and of a P granule reconstituted *in vitro* PGL-3^{488} and MEG-3^{647}. Scale bars are 500 nm and 3 μm respectively. Top panels are a maximum projection of a z-stack through the granule. Middle panels are a single X-Y plane through the middle of the same granule. Lower panels are a single Z-X plane through the middle of the same granule. See fig. S1 for additional examples of P granules captured *in vivo.*

B) *In vitro* time lapse series showing PGL-3^{488} droplets wetting the glass surface of a glass slide with 3 μM PGL-3, 80 ng/μL *nos-2* RNA, and the presence and absence of 0.5 μM MEG-3 (not shown). Average contact angles at 64s are indicated. Scale bar is 1 μm.

C) Contact angles for measured for droplets as in B. Each dot represents a droplet, red lines represent the mean.

D) *In vivo* time lapse series showing single molecules (green) of PGL-3::Halo and MEG-3::Halo in P granules (magenta). Scale bar is 1 μM.

E) Graph depicting the apparent diffusion coefficients of PGL-3::Halo and MEG-3::Halo molecules in P granules. Each dot represents one trajectory. Red line denotes the mean.

F) Graph depicting the dwell time of PGL-3::Halo and MEG-3::Halo molecules in P granules. Each dot represents one trajectory. Red line denotes the mean.

Fig. 2. MEG-3 reduces the surface tension of PGL-3 condensates and prevents coarsening.

A) Photomicrographs of PGL-3 droplets coalescing in the presence or absence of MEG-3.

B) Relaxation time of fusing PGL-3 droplets is plotted vs. length scale (ℓ) in the presence or absence of MEG-3. Each dot represents a single fusion event. The linear slope represents the inverse capillary velocity (η/γ).

C) Photomicrographs of a PGL-3 emulsion (max projections) at the indicated time points after assembly. 3 µM PGL-3 and 80 ng/µL *nos-2* RNA were incubated in condensation buffer in the presence or absence of 0.5 µM MEG-3 (not shown). Scale bar is 5 µm.

E and F) Histograms plotting the size distribution of PGL condensates assembled as in (C). Each data point indicates the fraction of total PGL-3 condensate volume represented by condensates binned by radius from 80 images (as in C) collected in 4 replicates. Lines were fit to a log normal distribution.

Fig. 3. MEG-3 stabilizes PGL-3 condensates against kinase accelerated coarsening.

A) Photomicrographs of a 2.5 µM PGL-3^{488} emulsion after 60min treatment with 100 nM DYRK-3 kinase in the presence of GTP (top panel) or ATP (bottom panel). Scale bar is 50 µM.

B) Histograms of PGL condensates assembled as in (A) with GTP/DYRK3 or ATP/DYRK3 at indicated time points. Circles indicate the number of PGL-3 condensates binned by the log(Intensity) of each condensate. Colors indicate the time after addition of DYRK-3.

C) Photomicrographs of PGL-3 condensates (max projections) assembled with and without 70 nM MEG-3 (green) and captured 60 min after addition of 100 µM ATP with and without 100 nM DYRK3. Arrows point to small PGL-3/MEG-3 condensates (see S4F and G for high resolution images). Inset is a high-resolution image with PGL-3 in magenta and MEG-3 in green. Scale bars are 50 µm and 5 µm (inset).

D) Diffusion coefficients of 200 nm microspheres in PGL-3 condensates with and without 100 nM DYRK3. Each dot represents a single microsphere trajectory. The red line represents the mean.

E) Histograms of PGL-3 condensates assembled with 70 nM MEG-3 and incubated for 60 min in 100 μM ATP with 100 nM DYRK3. Circles indicate the number of PGL- 3 condensates binned by the Log(Intensity) of each condensate captured from 17 images. See fig. S4D to E for additional MEG-3 concentrations and an extended time point.

Fig. 4. MEG-3/4 stabilize P granules against coarsening during the oocyte-to-zygote transition.

A) Schematics depicting the dissolution of P granules (magenta) during the transition from oocyte to fertilized zygote.

B) Photomicrographs of wild-type and *meg-3 meg-4* oocytes and zygotes expressing PGL-3::mCherry (white). Photomicrographs were captured in live adult hermaphrodites (*in utero*) or after dissection out of the uterus (*ex utero*). Representative photomicrographs are max projections corresponding to ~20% of oocyte volume and ~80% of zygote volume. The anterior (left) bias for PGL condensates in *meg-3 meg-4* zygotes correlates with anterior displacement of the oocyte nucleus (and associated P granules) that occurs immediately prior to fertilization. Scale bars are 10 μm.

C-F) Histograms of PGL condensate volumes measured from images captured as in A representing 100% of oocyte and zygote volumes. Circles indicate the volume of individual PGL-3 in condensates binned by condensate radius in wild-type (green) and *meg-3 meg-4* (black) oocytes and zygotes. Volumes are higher in F compared to E due to higher detection sensitivity *ex utero*.

G-H) Graphs showing the evolution of individual PGL condensates in a 10 min period starting after dissolution in wild-type and *meg-3 meg*-4 mutants under simulated conditions. Each line represents the evolution of the volume of a single condensate over time.

I-J) Graphs showing the average volume of individual PGL condensates in oocytes and zygotes under experimental and simulated conditions. I) Each dot corresponds to an oocyte (same data set as shown in D) or zygote (same data set as shown in F) of the indicated genotypes. J) Each dot corresponds to one simulation. Simulations were run in the presence or absence of the Pickering agent.

Fig. 5. MEG-3/4 drive asymmetric growth of the P granule emulsion during polarization.

A) Top row: Cartoons depicting PGL-3 condensates (red) and MEX-5 (grey) at different stages during the transition from unpolarized to polarized zygote. Bottom two rows: Photomicrographs of wild-type and *meg-3 meg-4* zygotes (*ex utero*) expressing PGL-3::mCherry and matching the stages shown in the cartoons above. Scale bar is 10 μm.

B-E) Graphs showing the total number (B-C) and total volume (D-E) of PGL-3::mCherry condensates in the posterior (light color) or anterior (dark color) half of wild-type and *meg-3 meg-4* zygotes calculated from photomicrographs as in A. Circles represent the average from 5 zygotes. Error bars represent the SD.

F-G) Graphs showing the rate of change in radius of PGL-3::mCherry condensates in wild-type and *meg-3 meg-4* zygotes calculated from traces as in H and I.

H-I) Graphs showing the evolution of individual PGL-3::mCherry condensates in anterior and posterior during polarization in wild-type and *meg-3 meg-4* zygotes. Traces begin at pronuclear formation and end just prior to pronuclear meeting.

J) Photomicrographs of fixed zygotes (mitosis) of indicated genotypes showing the distribution of MBK-2::OLLAS (green) and PGL-3::mCherry (magenta). Note that, in addition to P granules, MBK-2 localizes to centrosomes.

K) Graph showing the percent of PGL-3:mCherry condensates colocalized with MBK-2::OLLAS puncta in wild-type or *meg-3 meg-4* zygotes at the indicated developmental stages. Each circle represents one zygote (>50 puncta) and each line represents the mean.

L-M) Graphs showing the evolution of individual anterior (dark color) and posterior (light color) PGL-3 condensates under conditions simulating “wild-type" (starting condensate sizes as in wild-type zygotes, high conversion rate and Pickering agent) and “*meg-3 meg-4*” starting condensate sizes as

in *meg-3 meg-4* zygotes (starting condensate sizes as in wild-type zygotes, low conversion rate and no Pickering agent). Compare to experimental data in H and I.

Fig. 6. Pickering agents stabilize dynamic emulsions against kinase-accelerated coarsening

Schematics showing an idealized emulsion of a self-interacting polymer (blue).

A) In untreated condensates, polymer-polymer binding and unbinding events are slow (red dots), allowing the emulsion to persist with minimal coarsening over short time scales.

B and C) Phosphorylation by kinase increases solubility and accelerates internal dynamics (green dots in C). B) Under under-saturated conditions, kinase-accelerated dynamics causes the condensates to dissolve, as is observed in the anterior of wild-type polarized zygotes. C) Under saturated conditions, kinase-accelerated dynamics allow the condensates to rapidly grow by allowing new molecules from the dilute phase to enter the condensates. In the presence of the Pickering agent, the condensates are stabilized against coarsening, as observed in the posterior of wild-type polarized zygotes. In the absence of the Pickering agent, the condensates coarsen, as observed in *meg-3 meg-4* mutants during the oocyte-to-embryo transition. During polarization, MEG-3/4 function both as Pickering agents and recruiters of the kinase MBK-2. In *meg-3 meg-4* zygotes undergoing polarization, PGL condensates are maintained throughout the cytoplasm with minimal coarsening, because MBK-2 kinase is not recruited to the condensates and PGL dynamics remain slow as in A.

Science
AAAS

Supplementary Materials for

Pickering stabilization of a dynamic intracellular emulsion

Authors: Andrew W. Folkmann[1†], Andrea Putnam[1†], Chiu Fan Lee[2], and Geraldine Seydoux[1*]

Correspondence to: gseydoux@jhmi.edu

This PDF file includes:

Other Supplementary Materials for this manuscript include the following:

Materials and Methods

C. elegans strains

C. elegans were cultured according to standard methods (*51*). MEG-3, PGL-3, and MBK-2 were tagged at the endogenous locus with fluorescent or epitope tags using genome editing (*52*). Strains are listed in Table S1.

Laser scanning confocal microscopy

Super-resolution microscopy was performed using a Zeiss LSM 880 microscope equipped with a 63X-1.4 numerical aperture (NA) objective. Super-resolution images were acquired using ZEN software in SR mode, 1.8X zoom, and 0.15 µm Z-stack step size. Samples were illuminated with 488/561/637 nm solid-state laser, using a 488/561/633 transmitting dichroic (Zeiss) and a BP420-480+BP495-550 nm or P420-480+BP495-620 nm bandpass filter (Zeiss). The raw data was processed using default 3D Airyscan settings with ZEN software.

Spinning disk confocal microscopy

Super-resolution imaging of the PGL-3 emulsion *in vitro* and in eggs was performed using custom built inverted Zeiss Axio Observer with CSU-W1 SoRa spinning disk scan head (Yokogawa), 1X/2.8x/4x relay lens (Yokogawa), fast piezo z-drive (Applied Scientific Instrumentation), and an iXon Life 888 EMCCD camera (Andor). Samples were illuminated with 405/488/561/637 nm solid-state laser (Coherent), using a 405/488/561/640 transmitting dichroic (Semrock) and a 624-40/692-40/525-30/445-45 nm bandpass filter (Semrock). Images were taken using Slidebook software using a 40x-1.3NA/63X-1.4NA/100x-1.46NA objective (Zeiss) and a 1x, 2.8x, or 4x relay lens (Yokogawa) respectively depending on the sample. All spinning disk confocal imaging was performed in a climate controlled room kept at 18°C. See sections below for imaging analyses.

Near-TIRF single molecule microscopy

HaloTag labeling

HaloTag labeling was performed by feeding hermaphrodites expressing either MEG-3::Halo (EGD364) or PGL-3::Halo (JH3913) a concentrated OP50 culture (50 µl) containing 0.25 µM of JF_{549}-HaloTag ligand and 1 µM JF_{646}-HaloTag ligand on NNGM plates (IPM Scientific) for at least 3 hrs at

20°C. Hermaphrodites were washed 3x in M9 solution and dissected to release zygotes for mounting under a #1.5 22-mm square coverslip (170 ± 5 µm, Marienfeld) in 5 µl of M9 containing ~200 polystyrene bead (15.6 ± 0.03 µm diameter, Bangs labs). Two cell zygotes were chosen for analysis. Progression through the cell cycle is too fast in one cell zygotes to permit single molecule measurements.

TIRF Imaging (Fig. 1D)

Samples were simultaneously illuminated with 568 nm and 640 nm solid-state lasers and images were acquired in 'simultaneous' mode in the OMX Master software (GE Healthcare) on an DeltaVision OMX microscope with a Ring-TIRF module (GE Healthcare), 60x Olympus APO N TIRF/NA 1.49 oil objective and two front illuminated sCMOS cameras (PCO AG). For PGL-3::Halo (JH3913) time lapse images were acquired at an exposure of 100 ms or 150 ms at a time interval of 100 ms or 150 ms respectively. For MEG-3:Halo (EGD364) time lapse images were acquired at an exposure of 100 ms at a time interval of 500 ms or 1 s respectively. For all experiments, the ring diameter value, capture exposure setting, and time lapse frequency were chosen empirically to maximize signal intensity in each sample during the time course. (movies S1 and S2)

Single Molecule Analysis (Fig. 1E and F)

Single particle tracking of MEG-3::Halo (EGD364) and PGL-3::Halo (JH3913) was performed using the plugin TrackMate in Fiji (*53*). Feature size, and minimum intensity were empirically chosen so that >90% of the visible JF_{549} labeled particles were detected. Trajectories that occurred outside the JF_{646} labeled P granule area were manually excluded from analysis. 3D trajectory coordinates (x,y,t) were exported from Fiji. In some trajectories the JF_{646} labeled P granules themselves moved slightly within the zygote overtime. To account for this drift, JF_{549} particle trajectories were individually registered to the center of the JF_{646} labeled P granule using Excel (Microsoft). Trajectory coordinates were loaded into Matlab (MathWorks) for further analyses. Mean squared displacement (MSD) curves were calculated for each track with at least 5 consecutive frames using MSDanalyzer (*54*). Individual MSD curves were fitted to the equation $MSD = 4D_c t^{\alpha}$ with an R^2 of at least 0.8.

Protein and RNA purification

MEG-3 full-length (aa1-862) fused to an N-terminal 6XHis tag in pET28a was expressed and purified from inclusion bodies as described (*55*). MBP::6XHis::TEV::PGL-3 was expressed and purified as described (*29*) with the following modification. MBP was cleaved using homemade TEV protease instead of commercial. A plasmid expressing 8XHis::TEV::8XArg tag protease was obtained from Addgene (PRK793) and purified as described (*56*). Before loading cleaved PGL-3 protein on to a heparin

column (GE Healthcare), cleaved MBP::6XHis and 6XHis::TEV protease were removed using a HisTRAP column (GE Healthcare).

mRNAs were transcribed using T7 or SP6 mMessageMachine (Thermofisher) using manufacturer's recommendation as described (*55*). Template DNA for transcription reactions was obtained by PCR amplification from a plasmid containing the *nos-2* cDNA sequence (*55*). Free NTPs and protein were removed by lithium chloride precipitation. RNAs were resuspended in water and stored at −20°C. The integrity of RNA products was verified by agarose gel electrophoresis.

Protein labeling

Proteins were labeled with succinimidyl ester reactive fluorophores (Alexa Fluor™ 647 or DyLight™ 488 NHS Ester, Molecular Probes) following manufacturer instructions as described (*55*). Free fluorophore was eliminated by passage through three Zeba™ Spin Desalting Columns (7K MWCO, 0.5 mL) into protein storage buffer. The concentration of fluorophore-labeled protein was determined using fluorophore extinction coefficients measured on a Nanodrop ND-1000 spectrophotometer. Labeling reactions resulted in ~0.25-1 label per protein. Aliquots were snap frozen and stored. In condensation experiments, fluorophore-labeled protein was mixed with unlabeled protein for final reaction concentrations of ~12.5-50 nM of fluorophore labeled protein in the final reaction volume.

***in vitro* condensation experiments and analysis:**

Protein condensation was induced by diluting proteins out of storage buffer into condensation buffer containing 25 mM HEPES (pH 7.5), salt adjusted to a final concentration of 120 mM (30 mM KCl, 90 mM NaCl), and *nos-2* mRNA. Unless otherwise indicated, for co-assembly experiments 500 nM MEG-3, 3 µM PGL-3 and 80 ng/µL mRNA were used. PGL-3 and MEG-3 solutions contained 12.5-50 nM fluorescent trace labels with either Dylight™ 488, or Alexa Fluor™647 (indicated in figure legends).

PGL-3 wetting *in vitro* (Fig. 1B and C).

Condensation reactions were incubated in a 1.5 mL eppendorf tube for 30 min at room temperature (18°C) before spotting 15 µL onto a No. 1.5 glass bottom dish (Mattek). Fast 3D image stacks (0.2 µm Z steps, ~5 µm total) were captured every ~4 seconds using Slidebook software using a 63x oil objective and 1x relay lens. Time series Z stacks were exported from Slidebook software and further analysis was done in Imaris. Using the "Ortho" slicer functionality a 2D time series of images of the ZX plane (side view) for condensates wetting on the glass surface was generated. These images were

exported from Imaris and the interfacial angle at 64s post wetting was measured using the "Angle Tool" functionality in Fiji. Angle values for each condensate were exported from Fiji and statistically analyzed and graphed using GraphPad Prism.

PGL-3 coarsening and mixing *in vitro*

Condensation reactions were incubated in a 1.5 mL Eppendorf tube at room temperature (18°C) for indicated time points, before spotting 10 µL onto a No. 1.5 glass bottom dish (Mattek). 3D image stacks (5 µm Z steps) were captured using Slidebook software using a 63x oil objective and 1x relay lens (Fig. 2C, fig. S2E and I). For experiments containing dual labeled PGL-3 or MEG-3, condensation reactions containing 80 ng/µL *nos-2* RNA and 2.5 µM PGL-3 or 0.5 µM MEG-3 were trace labeled with either Dylight 488 or Alexa647 and incubated for 5 minutes. Then Dylight488 and Alexa647 containing reactions were mixed in equal volumes and incubated for indicated times. Single plane images were captured using Slidebook software using a 63x oil objective and 1x relay lens (fig. S3A). For experiments where excess PGL-3 was added, 2.5 µM PGL-3 trace labeled with Alexa647 and 80 ng/µL *nos-2* RNA with or without 0.5 µM MEG-3 were incubated for indicated times (0, 30s, 60 min) and then excess PGL-3 trace labeled with Dylight488 was added to the reaction (Final concentration 2.5 µM for a total of 5 µM PGL-3). 3D image stacks (5 µm Z steps) were captured using Slidebook software using a 63x oil objective and 1x relay lens (fig. S3D).

DYRK3/PGL-3 kinase assay

For kinase treatment final PGL-3 concentrations of 2.5 µM (Fig. 3A) and 5 µM (Fig. 3C) were utilized. Recombinant MEG-3 was added as indicated (50 nM, 70nM, 150 nM, and 250 nM). Recombinant GST::DYRK3 kinase was purchased ThermoFisher (#PV3837). Protein condensation was induced by diluting PGL-3 and MEG-3 (when applicable) out of storage buffer into condensation buffer containing 25 mM HEPES (pH 7.5), salt adjusted to a final concentration of 60 mM (15 mM KCl, 45 mM NaCl), and 1 mM DTT. Low salt conditions were required for efficient kinase activity, and no RNA was included. Condensation reactions were incubated in a 1.5 mL eppendorf tube at room temperature (18°C) for fifteen minutes. At the 15 minute time point a solution containing ATP or GTP (100 µM final), $MgCl_2$ (200 µM final), and DYRK3 (100 nM final) or DYRK3 kinase buffer (50 mM Tris (pH 7.5), 150 mM NaCl, 0.5 mM EDTA, 0.02% Triton X-100, 2 mM DTT, and 50% Glycerol). was added to the reaction, and further incubated at 30°C for sixty minutes. 15 µL of kinase reaction was spotted onto a No. 1.5 glass bottom dish (Mattek), 3D image stacks (5 µm Z steps starting at the coverslip) were captured using Slidebook software using a 40x oil objective and 1x relay lens. Images were exported from Slidebook software and further analysis was done in Fiji.. To examine the DYRK3 phosphorylation state of the PGL-3 samples, kinase treated samples were resuspended in 1x SDS sample buffer (minus EDTA)

and resolved via Phos-tag SDS-PAGE (Wako Chemicals, Japan). Migration of Alexa labeled proteins within the gel was visualized using non-confocal laser scanner (Typhoon 7000, GE Healthcare) (fig. S4A to C). To analyze the impact of DYRK3 phosphorylation on PGL-3 solubility, kinase treated samples were centrifuged at 13,000 r.p.m for 10 min. Supernatants and pellets were resuspended in 1X SDS sample buffer and resolved via SDS-PAGE (fig. S4B).

in vitro condensate image analysis and quantification

Images were exported from Slidebook software and further analyses was done in Fiji. Images used for quantification were single planes taken from a 5 image Z-stack starting at the surface of the glass dish. To quantify condensates, a mask was created by thresholding single plane images or max projections, smoothing once, filtering out objects of less than 4 pixels to minimize noise, applying a watershed filter to improve separation of objects close in proximity, and converting to a binary image by the Otsu method using the nucleus counter cookbook plugin. Minimum thresholds were set to the mean intensity of the background signal of the image plus 1-2 standard deviations. The maximum threshold was calculated by adding 4-6 times the standard deviation of the background. Using generated masks, the 2D area in μm^2 and the intensity of each condensate were measured and exported into Excel (Microsoft) for further analysis. Assuming that each condensate is a sphere in solution the radius (r) was determined from the 2D area μm^2 (A) measurement, $r = (A/\pi)^{0.5}$. This radius value was used to calculate 3D volume (v) and surface area (s.a.) for each condensate, $v = (4/3)\pi r^3$ and $s.a. = 4\pi r^2$. Objects from multiple images were identified and quantified as described above. Histograms of PGL-3 condensate volumes were generated by summing the volume binned by the radius of each PGL-3 object and normalized to the total volume of condensates in the reaction. Final data points are the average of 4 replicates (a total of 20 images per replicate, Fig. 2D and E, fig. S2F to H, and J to M). To quantify the mixing of PGL-3 condensates over time, the Pearson's correlation coefficient of PGL-3 intensities in the 488 or 647 channels was compared. Final data points are the average of 3 replicates (a total of 40 images per replicate for fig. S3B and C, and total of 3 images per replicate for fig. S3E and F).

For kinase assays, addition of the kinase resulted in the formation of large droplets that rapidly wet the surface of the coverglass resulting in inaccurate volume measurements. To compare the amount and distribution of condensates, histograms of PGL-3 condensate intensity were generated by taking the number of condensates binned by the intensity of each PGL-3 object. Final data points are the average a total of 4 images for Fig. 2B, a total of 17 images for Fig. 3E and a total of 5 images for fig. S4D to F).

Quantification of PGL-3/MEG-3 distribution in *in vitro* condensates

Super-resolution images were captured using Slidebook software using a 40x oil objective and 4x relay lens (fig. S4F). Line scans of intensity were measured for individual condensates. PGL-3 and MEG-3 intensities were normalized to the maximum intensity. To compare condensates of different sizes, PGL-3 intensities were manually analyzed using GraphPad Prism to determine the center and edge of the distribution. PGL-3 and MEG-3 intensities were normalized to a length scale from diameter of the PGL-3 condensate to ± 25% of the length and divided into 30 segments. Normalized distributions were plotted using GraphPad Prism as the median intensity of 5 condensates (figs. S4G).

PGL-3 microrheology experiments

Microrheology was performed by adding 200 nm diameter fluorescent microspheres with carboxyl surface chemistry (Invitrogen) to PGL-3 condensation reactions as described (*57*) . Microspheres were added to 3 µM PGL-3 condensation reactions with 80ng/µL *nos-2* RNA with and without 500 nM MEG-3 (Fig.S2A to D, and movie S3) or 5 µM PGL-3 condensation reactions with no RNA with and without 100 nM DYRK-3 kinase as described above (Fig. 3D, and movie S8). Condensate reactions were observed between 30-60 minutes after assembly. Time lapse movies were acquired using Slidebook software with a 100x oil objective and 4x relay lens, a 120 ms interval, and an exposure time of 5s. Images were acquired several µm above the coverslip to avoid interactions with the glass. Images were analyzed and individual microspheres were tracked using the Trackmate package in FIJI (*58*). Microspheres on or near the interface were excluded from the data analysis to avoid surface artifacts.

Tracks were imported into Matlab and the two-dimensional mean-squared displacement (MSD) was calculated as a function of lag-time using MSDanalyzer (*54*). MSD was calculated for tracks with length of ≥ 375 frames from multiple droplets for indicated conditions. The mean MSD was fit to $MSD = 4Dt^{\alpha}$ to calculate the apparent diffusion coefficient (D) and alpha component (α). The mean MSD grows linearly with time ($\alpha \approx 1$) indicating that the beads did not experience subdiffusive behavior. To obtain diffusion coefficients (D) for individual tracks, we fit the MSD data to MSD = 4Dt. The noise floor was determined experimentally for beads adhered to a coverslip to be $\approx 1.7 \times 10^{-5}$ µm^2. To calculate viscosity we used the Stokes-Einstein equation ($D=k_BT/6\pi\eta a$) where k_B, is the Boltzmann constant, T is the temperature, η = viscosity, and a is the diameter of the microsphere. Calculated viscosities are similar but somewhat slower than previously reported values (*2*, *59*), which is consistent with the lower temperature (18°C), and salt (120 mM (reactions without kinase), 60 mM (kinase reactions). Reported viscosities are averages ± 95% confidence interval.

PGL-3 coalescence experiments

PGL-3 droplet coalescence was performed by imaging condensation reactions containing 2.5 µM PGL-3 with 80 ng/µL *nos-2* RNA with and without indicated concentrations of MEG-3 under conditions

described above (Fig. 2A and B, and movies S4 to S7). PGL-3 condensate reactions were observed between 30-60 minutes after assembly. Time-lapse movies were acquired using Slidebook software with a 60x oil objective and 1x relay lens, a 120 ms interval, and an exposure time of 20s. Images were acquired several µm above the coverslip to avoid condensates wetting the glass coverslip. The aspect ratio, AR, of nucleoli was determined by fitting an ellipse to the shape and calculating AR = L/S, where L and S are the long and short axes of the ellipse using a custom Matlab script (*60*). For analysis of fusing PGL-3 droplets, the change in aspect ratio over time was fit to a function $AR = AR_f + (AR_o - AR_f)\cdot e^{(-t/\tau)}$, where t is time, τ is the relaxation time, and AR_o and AR_f are the initial and final aspect ratios respectively. AR_f were constrained to values ≥ 1 during fitting. The length scale of condensates was defined as the geometric mean where $\ell = [(L_o - S_o)\cdot S_o]^{½}$. Plots of τ vs. ℓ were fit to a line of the form $\tau = \ell(\eta/\gamma)$, to determine the inverse capillary velocity η/γ.

Live imaging experiments and analysis

Since the PGL-3 emulsion is temperature sensitive, live imaging was performed at 18°C, a temperature that preserves the integrity of PGL-3 condensates in wild-type (JH3914) and *meg-3 meg-4* (JH3915) zygotes (fig. S7A and B). Oocyte maturation and fertilization cannot occur *ex vivo* and therefore must be analyzed in hermaphrodites (*in utero*). Zygotes that have completed meiosis can develop outside of hermaphrodites, and therefore were analyzed after dissection (*ex utero*) to maximize the sensitivity of fluorescence imaging.

in utero analyses

Adult hermaphrodites (JH3914, JH3915) were washed 2x in L-15 (Gibco) solution and were immobilized on a 35mm, No. 1.5 glass bottom dish (Mattek) in a L-15 medium containing 20 µm polystyrene beads (Polysciences) and 1 mM levamisole (Sigma). 3D image stacks spanning the entire germline and uterus (0.2 µm Z steps) were taken at max laser intensity using Slidebook software using a 40x oil objective and 2.8x relay lens (Fig. 4B). Images were exported from Slidebook and imported into Imaris image analysis software for further analysis. Individual oocytes and zygotes were isolated using the "Surface" functionality. The "Spot" functionality was used to identify P granules and statistically code the 3D sphere volume ($µm^3$) of each identified P granule within a zygote. Individual condensate volume values for P granules for each zygote were exported from Imaris and statistically analyzed and graphed using GraphPad Prism (Fig. 4C to E, fig. S5A). To calculate the total intensity of PGL-3 in oocyte and zygotes Imaris generated "Surfaces" were exported to Fiji. Images were background

corrected and the total intensity was summed. The total intensity of each sample was then normalized to the average intensity of the sample (fig. S5B).

ex utero analyses

Adult hermaphrodites expressing endogenous PGL-3::mCherry (JH3914, JH3915) were washed 2x in L-15 (Gibco) solution and dissected to release the zygotes into ~100 µl L-15 (Gibco) solution on a 35mm, No. 1.5 glass bottom dish (Mattek) image stacks (0.2 µm Z steps, 10 µm total) were taken at max laser power at indicated developmental time points using Slidebook software using a 40x oil objective and 4x relay lens (Fig. 4B, Fig 5A). Images were exported from Slidebook and imported into Imaris image analysis software for further analysis. In Imaris the "Spot" functionality was used to identify all P granules within the zygote and statistically code the 3D sphere volume (μm^3) of each identified P granule. Individual condensate volume values for P granules for each zygote were exported from Imaris and statistically analyzed and graphed using GraphPad Prism (Fig. 4F, and fig. S6A and B). To calculate the total intensity of PGL-3 images were exported to Fiji. Images were background corrected and the total intensity was summed (fig. S6C). To quantify the number of condensates in the anterior of posterior of the zygote (JH3918 and JH3919), images were exported to Fiji. Using a maximum projection, a mask was created to identify PGL-3 condensates by smoothing, thresholding, filtering out objects of less than 2 pixels, applying a watershed filter to improve separation of objects close in proximity, and converting to a binary image by the Otsu method using the nucleus counter cookbook plugin. Using generated masks, the number and the area of each condensate was calculated. Assuming that each condensate is a sphere in solution the radius (r) was determined from the 2D area μm^2 (A) measurement, $r = (A/\pi)^{0.5}$. This radius value was used to calculate 3D volume (v) and surface area (s.a.) for each condensate, $v = (4/3)\pi r^3$ and $s.a. = 4\pi r^2$. Condensates were split into either anterior or posterior half of the zygote, and plotted by stage (Fig. 5B to E).

Live tracking of P granules

Live tracking of P granules in oocytes was not possible due to high photosensitivity and movement of the eggs from the oviduct to the spermatheca and into the uterus. Live tracking in zygotes (JH3914, JH3915) was performed *ex utero* by acquiring 3D image stacks (0.6 µm Z steps, 12 µm total) every ~5 seconds using Slidebook software using a 100x/1.46NA oil objective and 1x relay lens. Time series images were exported from Slidebook software. Images were corrected for photobleaching using the "Bleach Correction" feature in Fiji and further analyses were done in Imaris. Individual P granules were identified using the "Spot" functionality in Imaris. Spots were tracked over time using the Imaris "Autoregressive Motion" algorithm. Tracks were manually inspected and corrected if required. Volume and Z-coordinate values were exported from Imaris for further analysis in excel and graphed using

GraphPad Prism. All tracks that were less than 5 frames, entered or exited the Z-plane during imaging, or moved from the posterior to the anterior (or the reverse) during imaging were discarded. To calculate the rate of change in size, radius was calculated from the volume for each P granule. The slope of the change in radius over time was calculated and plotted using GraphPad Prism (Fig. 5F to I, and movie S9).

Immunostaining and analysis:

For direct fluorescence imaging of MEG-3::GFP and PGL-3::mCherry (Fig. 1A and fig. S1A), gravid adult hermaphrodites (JH3921) were placed on #1.5 22x22 mm coverslip (170 ± 5 µm, Marienfeld) coated with 0.1% poly-L-lysine (Sigma) in a L-15 medium containing 25 µm polystyrene beads (Polysciences). The zygotes were extruded by squashing hermaphrodites with an opposing #2 24x50 mm glass coverslip (VWR) and snap frozen in liquid nitrogen. The 24x50 mm coverslip was removed and zygotes were permeabilized by incubation in chilled methanol at -20°C overnight. Coverslips were then rehydrated in PBST/BSA (0.1% PBS-Tween 0.5% BSA) at room temperature for at least 3 hours. Coverslip were mounted onto a 25x75x1 mm microscope slide (ThermoFisher Scientific) in ~5 µl of antifade mounting medium (VectaShield). 3D image stacks (0.15 µm Z steps) were taken at indicated developmental time points using ZEN software using a 63x oil objective (Zeiss). To quantify the distribution of PGL-3 and MEG-3 fluorescence within a condensate, line scans of intensity were measured for individual condensates. PGL-3 and MEG-3 intensities were normalized to the maximum intensity. To compare condensates of different sizes, PGL-3 intensities were fit to a gaussian curve using GraphPad Prism to determine the center and the standard deviation of the distribution. PGL-3 and MEG-3 intensities were normalized to a length scale from the center of the distribution to ± 4 standard deviations and divided into 30 segments. Normalized distributions were plotted using GraphpPad Prism as the median or max intensity of 39 condensates, or as representative single condensates (fig S1B to D).

For immunostaining of OLLAS::MBK-2 and PGL-3::mCherry (Fig. 5J, and fig. S6F), gravid adult hermaphrodites (JH3916, JH3917) were placed on #1.5 22x22 mm coverslip (170 ± 5 µm, Marienfeld) coated with 0.1% poly-L-lysine (Sigma) in a L-15 medium containing 25 µm polystyrene beads (Polysciences). The zygotes were extruded by squashing hermaphrodites with an opposing #2 24x50 mm glass coverslip (VWR). These zygotes were snap frozen in liquid nitrogen. The 24x50 mm coverslip was removed and zygotes were permeabilized by incubation in chilled methanol at -20°C overnight. Coverslips were then blocked in PBST/BSA at room temperature for at least 3 hours and incubated with Rat αOLLAS-L2 (1:200, Novus Biological Littleton, CO) at 4°C overnight. Following primary incubation, the coverslips were extensively washed with TBST. Secondary antibodies anti-Rat Alexa Fluor 488 (LifeTech) were diluted in PBST/BSA applied to coverslips at room temperature.

Following secondary incubation, the coverslips were extensively washed with PBST. Coverslip were mounted onto a 25x75x1 mm microscope slide (ThermoFisher Scientific) in ~5 µl of antifade mounting medium (VectaShield). 3D image stacks (0.2 µm Z steps) were taken at indicated developmental time points using Slidebook software using a 40x oil objective and 4x relay lens. Images were exported from Slidebook software and further analyses was done in Imaris. In Imaris the "Spot" functionality was used to identify all MBK-2 and PGL-3 puncta within the zygote and statistically code the 3D sphere volume (μm^3). Using the 'measure' functionality, a nearest neighbor measurement from the center of these statistically coded MBK-2 and PGL-3 condensates was performed. PGL-3 and MBK-2 condensates that were within 500 nm were considered colocalized and counted. These values were exported from Imaris and statistically analyzed and graphed using GraphPad Prism (Fig. 5K). Percent colocalization = (Total # colocalized PGL-3 & MBK-2 condensates) / (Total # PGL-3 condensates) X 100.

For immunostaining of endogenous MEG-3::OLLAS and untagged PGL-3 (fig. S6D), gravid adult hermaphrodites (JH3477) were placed on a custom-made chambered slide (ThermoFisher) coated with 0.1% poly-L-lysine (Sigma), and zygotes were extruded by squashing with a glass coverslip. Zygotes were frozen on pre-chilled aluminum blocks for 5 min. The coverslip was removed, and zygotes were permeabilized by incubation in chilled methanol at -20°C for 15 min followed by incubation in chilled acetone -20°C for 10 min. Slides were then blocked in PBST/BSA at room temperature and incubated with primary antibodies at 4°C. Antibodies were diluted in PBST/BSA as follows: KT3 (1:10, DSHB), Rat αOLLAS-L2 (1:200, Novus Biological Littleton, CO). Primary antibodies were applied sequentially (OLLAS before KT3) to avoid cross reaction. Secondary antibodies Anti-Mouse DyLight 650 (Abcam) and anti-Rat Alexa Fluor 488 (LifeTech) were diluted in PBST/BSA applied to slides at room temperature. Zygote were mounted under a #1.5 22-mm square coverslip (170 ± 5 µm, Marienfeld) in ~5 µl of antifade mounting medium (VectaShield). 3D image stacks (0.2 µm Z steps) were taken at indicated developmental time points using Slidebook software using a 40x oil objective and 4x relay lens.

To quantify the ratio of MEG-3 or MBK-2 to PGL-3 signal in the zygote (fig. S6E and G), images were exported to Fiji. For MEG-3/PGL-3 images, maximum projections were analyzed. For MBK-2/PGL-3 images, single planes spaced 1.6 µm apart were analyzed because the cytoplasmic background signal of MBK-2 was high relative to the intensity of MBK-2 in condensates. For both data sets a mask was created to identify PGL-3 condensates by smoothing, thresholding, filtering out objects of less than 2 pixels, applying a watershed filter to improve separation of objects close in proximity, and converting to a binary image by the Otsu method using the nucleus counter cookbook plugin. Using generated masks, the integrated intensity within each object for both PGL-3 and MBK-2 or MEG-3 channels was calculated. To remove non-specific background signal the mean intensity of an image field

calculated from a region outside of the zygote was subtracted from each pixel. The intensity of each condensate was divided by the intensity of the zygote to normalize to different staining efficiencies. The ratio of MBK-2 or MEG-3 to PGL-3 was calculated for each condensate and plotted versus the position on the anterior/posterior axis for multiple zygotes at each stage.

in silico modeling

For the oocyte to zygote simulation, 3 sets of starting condensate radii were generated from experimentally observed data (Fig. 4C). Using the mathematical formalism described in the Supplemental Text, the change in condensate radii was modeled over a 10 min window using a custom MatLab (MathWorks) program. This time window corresponds to fertilization of the oocyte and passage through the spermatheca into the uterus of the animal. To graphically display the simulation results, the radii output generated in MatLab (MathWorks) of individual condensates were converted to spherical volumes using Excel and plotted over time using GraphPad Prism. To display the size distributions of the simulated condensates, histograms of condensate volume were generated by summing the volume binned by the radius of each condensate at the start and end of the simulation.

For the polarization simulation, a representative starting P granule size distribution was generated from experimentally observed data (Fig. 5A) for both wild-type and *meg-3 meg-4* genotypes. The simulations shown in (Fig. 5L, and fig. S6I to K) used a wild-type starting radii distribution, and simulation shown in (Fig. 5M) utilized a *meg-3 meg-4* starting radii distribution. Using the mathematical formalism described in the Supplemental Text, the change in condensate radii was modeled over a 6 min window using a custom MatLab (MathWorks) program. This time window corresponds to time frame encompassing the initiation of polarization at pronuclear formation until the zygote is polarized at pronuclear meeting. To plot the simulation results, output radii were converted to spherical volumes using Excel and plotted over time using GraphPad Prism. To visualize simulations results, output radii were converted to spherical volumes and randomly distributed in the anterior or posterior of an idealized zygote and visualized over time. Text and animation were added to these time series using Premiere Pro (movie S10).

Analysis software

Excel (Microsoft) and GraphPad Prism v9 were used for all data analysis and graphing. Images were captured with Slidebook v6 (Intelligent Imaging Innovations) or Zen Black (Zeiss). Fiji v1.52g, Imaris v9.51 (Bitplane), Matlab v2017b and v2021a (Mathworks), and Zen Blue (Zeiss) were used for image

processing and analysis. Matlab v2019b (MathWorks) was used for all *in silico* simulations. Premiere Pro v14.8 (Adobe) was used for video editing.

Supplementary Text

Introduction to emulsions

Emulsions are collections of liquid condensates that co-exist in a common medium (fig. S8A). We describe how liquid emulsions evolve over time.

Diffusion-limited emulsions:

Consider a simple polymer with several low-affinity binding sites (fig. S8B). The binding sites allow polymer molecules to bind to each other reversibly to form extended dynamic networks of weakly interacting molecules. At low concentration, polymer molecules exist primarily as dispersed soluble monomers. Above a certain concentration ("critical concentration"), polymer molecules phase separate and redistribute into dense condensates surrounded by a more dilute phase (*1*). Molecules in the condensates are bound dynamically to each other in a network that is constantly remodeling. Molecules in the dilute phase are free to diffuse and, when near the condensate surface, interact with molecules in the condensates. The **conversion rate** refers to the rate at which new molecules near the surface are incorporated into the condensate.

In highly dynamic emulsions, the conversion rate is faster than the rate of diffusion-limited adsorption of molecules to the surface of the condensate (**"diffusion-limited"**). In a diffusion-limited system, exchange of molecules between the dilute and condensed phases can occur rapidly (the probability that a molecule near the surface is incorporated into the condensate is high). In diffusion-limited emulsions, the entire condensate volume can exchange with the dilute phase over short time scales.

Conversion-limited emulsions:

Recently, theoretical and experimental observations have indicated that certain polymer condensates evolve into less dynamic states overtime (*2*, *61*, *62*). As binding interactions increase between polymers in the condensates, the polymers become more and more engaged with each other and less free to engage in binding interactions with molecules in the dilute phase (*2*, *8*, *63*). As the binding sites saturate, the conversion rate falls below the diffusion-dependent adsorption rate of new monomers to the condensate surface. This makes it more difficult for molecules to enter the condensates (*2*, *8*). Under such **"conversion-limited"** scheme, exchange still occurs between the condensate and dilute phases, but net incorporation of new molecules into condensates slows down. We have used such a "conversion-limited" scheme to model the PGL emulsion given the relatively high viscosity of PGL-3 droplets *in vitro*

and our observations of PGL dynamics *in vivo* (see below under justification for assumption 1 in the model).

Coarsening:

Molecules at the condensate surface make fewer favorable binding interactions with their neighbors and thus are energetically less stable than molecules deep inside the condensates. The energy associated with this difference is called surface tension. To minimize surface tension, emulsions tend to minimize overall interfacial area by favoring the growth of larger condensates (which have low surface-to-volume ratios) over that of smaller condensates (which have high surface-to-volume ratios). This thermodynamic evolution is called **coarsening** (fig. S8A).

Two mechanisms drive coarsening: 1) coalescence (fusion) of condensates and 2) Ostwald ripening. Ostwald ripening refers to the preferential exchange of molecules from small to large droplets (fig. S8C). Overtime small condensates are absorbed into large condensates until eventually the emulsion reduces to one large condensate (*64*).

The rate of coarsening depends on the surface tension, the solubility and diffusion rate of the polymer in the dilute phase, and the conversion rate. Coarsening driven by coalescence additionally requires interaction between condensates and depends on the density and diffusion of condensates. Increase in any of these parameters will increase the rate of coarsening and lead to fewer, larger condensates in a shorter time.

Regulation of coarsening in cells:

Several mechanisms have been proposed to regulate coarsening in cells. Reversible modifications (ie. phosphorylation) that transiently weaken binding interactions will increase the number of molecules in the condensate available for binding and thus increase the conversion rate (*65*). Modifications can also increase the solubility of polymer molecules in the dilute phase, thus increasing shedding of molecules by smaller condensates and Ostwald ripening (*64*).

Cellular structures that keep condensates away from each other prevent coalescence and slow down coarsening way (*5*, *12*, *66*). For example, an F-actin network stabilizes an emulsion of hundreds of nucleoli in *Xenopus laevis* oocytes, but when actin is disrupted, the emulsion rapidly coarsens (*5*). Coarsening has also been proposed to be reduced in the presence of cytoplasmic gradients that counteract Ostwald ripening by controlling diffusion in the dilute phase (*15–18*, *67*). Active mechanisms that continuously regenerate small condensates will also counteract coarsening (*18*).

In this study, we identify a new mechanism for coarsening regulation in cells by showing that the intrinsically disordered protein MEG-3 functions as a Pickering agent for P granules, liquid condensates

in *C. elegans* zygotes. Pickering agents were first described in the context of inorganic emulsions by Ramsey and Pickering (*19*, *20*). Working with oil in water emulsions, Ramsey and Pickering discovered that small inert particulates such as clay greatly slow down coarsening. **"Pickering agents"** are particulates ranging from 0.1 - 100 μm in diameter and are typically at least an order of magnitude smaller than droplets in the emulsion (*40*). They can be wetted by both the condensed and dilute phases leading to strong interfacial adsorption (*40*). The adsorption energy creates an energetically favorable counterbalance to the surface tension cost, effectively neutralizing the primary drive for coarsening (fig. S8A).

Theoretical model

Model assumptions

The key model assumptions are:

1. PGL-3 condensates coarsen under the conversion-limited scheme. We ignore coarsening by coalescence and fusion, as these events are infrequently observed experimentally *in vivo*.
2. MEG-3 clusters localizing to the surface of PGL-3 condensate reduce surface tension (Pickering effect).
3. PGL-3 condensate conversion dynamics are accelerated by unknown factors during the oocyte to zygote transition and by MEG-3-dependent recruitment of MBK-2 to PGL-3 condensates during polarization.
4. During polarization, PGL-3 condensates experience i) spatially differential surface tensions due to enrichment of MEG-3 in the posterior and ii) spatially differential levels of supersaturation due to enrichment of MEX-5 in the anterior.

Justifications for model assumptions

Assumption 1:

PGL-3 condensates coarsen under the conversion-limited scheme. We ignore coarsening by coalescence and fusion, as these events are infrequently observed experimentally in vivo.

In the standard diffusion-limited Ostwald coarsening kinetics, the governing equations are given by (*68*, *69*)

$$\frac{dR_i(t)}{dt} = \frac{A}{R_i}\left(\epsilon(t) - \frac{l_c}{R_i(t)}\right), \quad (1)$$

where $R_i(t)$ denotes the radius of the i-th condensate in the system, the Gibbs-Thomson length scale l_c is proportional to the surface tension and quantifies the effects of surface tension on the coarsening kinetics. Also, A is a constant quantifying the kinetic rate, and $\epsilon(t)$ is the dimensionless supersaturation level given by:

$$\epsilon(t) \equiv \frac{c(t)}{c_{\text{out}}} - 1\,, \tag{2}$$

with $c(t)$ being the far-field concentration in the dilute phase and c_{out} is the equilibrium concentration in the dilute phase right outside a flat interface.

Using reasonable parameters from the literature shown in Table 1, this standard scheme predicts a coarsening kinetics much faster than experimental observations. Motivated by recent simulation work showing that biomolecular condensates are likely to be in slow kinetics (e.g., glassy) states (*70*, *71*), we do not employ the standard scheme above. Instead, we assume here that condensate coarsening kinetics is conversion-limited, which applies when the absorption and desorption time scales of a molecule into and out of a condensate are much slower than the time scale of homogenization of concentration in the cytoplasm due to diffusion (fig. S8C). Specifically, the kinetics equations in this conversion-limited regime are of the form:

$$\frac{dR_i(t)}{dt} = K\left(\epsilon(t) - \frac{l_c}{R_i(t)}\right). \tag{3}$$

where K is a kinetic rate that is independent to R_i (unlike the standard formulation) due to the fact that the growth/shrinkage of condensates is no longer diffusion-limited.

A physical mechanism that can lead to slow absorption and desorption time scales is the inherent slow internal dynamics in the condensates, which can be caused by multi-valent interactions of protein domains. Specifically, the binding and unbinding of protein domains within the condensates can lead to a rugged energy landscape that can drastically slow down the dynamics of molecular rearrangements (fig. S8D). However, the binding and unbinding rates can be further regulated by ATP-driven processes. Specifically, the binding and unbinding of protein domains can be slow when caused purely by thermal fluctuations, but fast when induced by a phosphorylation/de-phosphorylation cycle. The latter mechanism can be a basis of a kinase-controlled kinetic rates of condensate dynamics.

Assumption 2

MEG-3 clusters localizing to the surface of PGL-3 condensates reduce surface tension (Pickering effect).

This is supported by the experimental observations that MEG-3 clusters coat the surface of PGL-3 condensates *in vivo* and *in vitro*, and reduces PGL-3 surface tension by >4 -fold in reconstitution experiments *in vitro*.

Assumption 3

PGL-3 condensate conversion dynamics are accelerated by unknown factors during the oocyte to zygote transition and by MEG-3-dependent recruitment of MBK-2 to PGL-3 condensates during polarization.

This assumption is supported by examination of P granule dynamics in wild-type and *meg-3 meg-4* mutants (Fig. 4A to E) and additional genetic data presented in Wang et al. (*28*) (summarized below).

Oocyte to zygote transition: PGL-3 condensates dissolve in maturing oocytes, and this dissolution is observed in both wild-type and *meg-3 meg-4* mutants (Fig. 4). These observations indicate that accelerated PGL-3 dynamics at this stage do not require *meg-3* or *meg-4*. Previous genetic studies have also shown that the DYRK kinase MBK-2 is not required for P granule dissolution at this stage (*28*). The factors that induce P granule dissolution at this stage are not known.

Polarization: In polarizing zygotes (pronuclear formation to pronuclear meeting), most P granules in the anterior cytoplasm dissolve and many P granules in posterior cytoplasm grow. These dynamics are greatly reduced in *meg-3 meg-4* mutants (Fig. 5). Prior genetic studies have shown that P granule dynamics at this stage also require the DYRK kinase MBK-2 (*28*). In zygotes lacking MBK-2, P granules do not dissolve in the anterior cytoplasm. MBK-2 is opposed by the phosphatase $PP2A^{pptr\text{-}½}$. In zygotes lacking $PP2A^{pptr\text{-}½}$, the opposite phenotype is seen: P granules dissolve throughout the cytoplasm of polarizing zygotes. Strikingly, the “hyper-dissolution” phenotype of zygotes lacking $PP2A^{pptr\text{-}½}$ can be suppressed by reducing either *mbk-2* or *meg-3* (*28*). These genetic results indicate that MEG-3/MEG-4 are required for MBK-2 activity on P granules. These findings are consistent with our observation that MEG-3 and MEG-4 are required to recruit high levels of MBK-2 to P granules during polarization (Fig. 5J).

Assumption 4

During polarization, PGL-3 condensates experience i) spatially differential surface tensions due to enrichment of MEG-3 in the posterior and ii) spatially differential levels of supersaturation due to enrichment of MEX-5 in the anterior.

Assumption 4i) follows from Assumption 2 and the observation that MEG-3 becomes progressively depleted from anterior PGL-3 condensates during polarization (fig. S6D and E).

Assumption 4ii) follows from known effects of MEX-5 (*59*, *72*) which has been shown to increase the critical concentration for PGL-3 condensation in anterior cytoplasm, possibly by competing for RNA (which enhances PGL-3 condensation *in vitro*). This assumption is also supported by simulation results that demonstrate that, in the absence of a lower supersaturation state for anterior condensates, large PGL-3 condensates in the anterior grow transiently due to Ostwald ripening (fig. S6J), a behavior not observed in zygotes (Fig. 5H).

Modeling Oocyte (O) to Zygote (E) transition

Wild-type

Here, we focus on the last 10min of the O to E transition, which marks the initiation of coating of MEG-3 onto PGL condensates. Since the MEX-5 gradient is not yet present and MEG-3 is uniformly distributed, all condensates are treated as equal and the kinetic equations are given by (3), except to model non-instantaneous adsorption of MEG-3 clusters onto the PGL surface, we assume that the Gibbs-Thomson (GT) length scale l_c decreases from $l_c(t = 0) = 15$ nm to $l_c(t = 600\ \text{sec}) = 0.15$ nm according to the following equation:

$$l_c(t) = (15\text{nm} - 0.15\text{nm})e^{-\frac{t}{\tau}} + 0.15\text{nm}$$

where $\tau = 30$ sec. The temporal scale τ sets the time scale of MEG-3 cluster adsorption onto the PGL surface, and the value chosen is motivated by the experiments showing that adsorption is evident within one minute. The small value of the final Gibbs-Thomson length scale $l_c(t = 600\ \text{sec}) = 0.15$ nm adopted here is due to Pickering effects of MEG3 clusters on PGL condensate surface. We have performed a parameter sweep to illustrate the sensitivity of this parameter (see below).

The initial condensate size distribution is generated based on size distributions observed experimentally. Since most PGL-3 condensates shrink and the overall PGL-3 condensate volume decreases throughout the O to E transition, the cytoplasmic PGL-3 concentration at the beginning of the simulation is expected to be below the cytoplasmic concentration that corresponds to the steady state of a condensate of an average size. Specifically, we define such steady state concentration c_{ss} to be such that $\frac{d\langle R\rangle}{dt} = 0$, where $\langle R\rangle$ denotes the average radius of a given collection of condensates. From (3),

$$c_{ss} = c_{out}\left(\langle\frac{l_c(t=0)}{R(t=0)}\rangle + 1\right). \quad (5)$$

Using this concentration as the reference, we set our initial cytoplasmic concentration to be $0.96 \times c_{ss}$.

The only remaining parameter is the kinetic rate K. Since variations in growth/shrinkage kinetics are clearly observed experimentally, we include these variations in the kinetic equations by having condensate specific kinetic rate. Specifically, the i-th condensate's kinetic rate is given by

$$K_i = \kappa\left(K + \frac{K}{2}r_i\right), \quad (6)$$

where K is set to be 10 nm/s, and r_i is a random number generated uniformly between -1 and 1. The variation in the kinetics can again be justified by the variable rugged energy landscapes in distinct condensates (fig. S8D). In addition, since MEG-3 clusters on the surface diminish a PGL-3 monomer's access to the PGL-3 condensate, the rate is reduced as a result, which is modeled by the presence of the prefactor κ, taken to be

$$\kappa(t) = (1-0.2)e^{-\frac{t}{\tau}} + 0.2 \quad (7)$$

which has the same temporal trend as the Gibbs-Thomson length scale l_c.

Mutant

For the mutant case, all parameters are identical to WT, except that since MEG-3 is absent, the capillary length returns to the expected value of $l_c = 15$ nm, and the prefactor κ is no longer present. However, variations in the kinetic rates remain and the expressions are given by:

$$K_i = K + \frac{K}{2}r_i\,. \quad (8)$$

The simulation predicts a slight increase in PGL-3 volume in wild-type zygotes compared to *meg-3 meg-4* zygotes which is not observed experimentally. This suggests that MEG-3 may increase the solubility of PGL-3 slightly *in vivo*. For simplicity, we did not include this in the model.

Parameter sweeps

In this section, we scan the key parameters to identify the range of model parameters that exhibit system behavior consistent with experimental observation. The key parameters that are not based on experimental inputs are the reduced Gibbs-Thomson length scale $l_c^{Pickering}$ due to Pickering effects and the kinetic rate K. In the left figure below, we scan both $l_c^{Pickering}$ and K in the case of WT and plot the resulting ratio of the mean radius of the condensates at $t = 600$ sec vs that at $t = 0$ sec, i.e., $R^{t=600s}/R^{t=0s}$. In fig. S9A and B we scan a range of the kinetic rate K and focus on $R^{t=600s}/R^{t=0s}$.

Compared to experimental observation, results in the mutant case indicates that the kinetic rate K is expected to be below 25 nm/s for $R^{t=600s}/R^{t=0s}$ = 0.5-0.6 (fig. S9B). Within this range, the WT result at $R^{t=600s}/R^{t=0s}$ = 1-1.2 indicates that the $l_c^{Pickering}$ is below 6 nm (fig. S9A) which shows that it $l_c = 15\ nm$) be at least half of the value of the $l_c^{Pickering}$ without Pickering. In other words, we expect that the surface tension is decreased by at least 50% due to Pickering effects. This expectation has been borne out by *in vitro* experiments reported in Fig. 2, where MEG-3 is observed to reduce the surface tension of PGL-3 droplets by at least 4-fold.

Modeling Pronuclear Formation (PF) to Pronuclear Migration (PM)

Wild-type

Just prior to PM, condensates are quickly nucleated. MEG-3 clusters are initially found on all condensates and progressively relocalize from anterior to posterior (fig. S6A and B). In the simulation, we assume that all posterior PGL-3 condensates are coated by MEG-3 clusters, while anterior PGL-3 condensates are not.

Due to the Pickering effect of MEG3 clusters on the PGL condensates, $l_{c,P} \ll l_{c,A}$. Specifically, as in the O to E transition, we assume that $l_{c,A} = 15$ nm and $l_{c,P} = \frac{l_{c,A}}{100} = 0.15$ nm. Since the anterior and posterior condensates have distinct properties in this case, the kinetic equations are:

$$\frac{dR_{A,i}(t)}{dt} = K_{A,i}\left(\epsilon_A(t) - \frac{l_{c,A}}{R_{A,i}(t)}\right) \quad (9)$$

$$\frac{dR_{P,i}(t)}{dt} = K_{P,i}\left(\epsilon_P(t) - \frac{l_{c,P}}{R_{P,i}(t)}\right) \quad (10)$$

where the subscripts A, P refer to whether the condensates are in the anterior or posterior, respectively.

Furthermore, similar the O-to-E transition, the kinetics parameters are defined as follows:

$$K_{A,i} = K + \frac{K}{2} r_{A,i} \tag{11}$$

$$K_{P,i} = \kappa \left(K + \frac{K}{2} r_{P,i} \right) \tag{12}$$

where $K = 12$ nm/sec and $r_{A,i}, r_{P,i}$ are again random numbers picked uniformly between -1 and 1. Compared to *meg-3 meg-4* mutants, the kinetic rate K is higher in wild-type due to the fluidization effects of MEG-3 in the system (assumption 3).

In (7) and (8), the supersaturation levels $\epsilon_{A/P}$ also differ in the two sides of the cytoplasm due to the MEX-5 gradient (assumption 4). Here, we assume that $c_{A,\text{out}} = 1.2 \times c_{P,\text{out}}$ (see Eq. (2)) so that solubility of PGL-3 is higher in the anterior.

To set the initial cytoplasm PGL-3 concentration, we again first consider the steady state concentration for the average condensate size at the beginning of the simulation, which is given by

$$c_{\text{ss}} = c_{P,\text{out}} \left[\frac{N_A}{N_{\text{tot}}} \left\langle \frac{l_{c,A}}{R_{A,i}(t=0)} \right\rangle + \frac{N_P}{N_{\text{tot}}} \left\langle \frac{l_{c,P}}{R_{P,i}(t=0)} \right\rangle + 1 \right]. \tag{13}$$

Since condensates are nucleated at the beginning of the PF stage, the cytoplasmic PGL-3 concentration is expected to be above c_{ss}. In our simulation, we assume that $c(t=0)$ is 10% above c_{ss}.

Parameter sweeps (WT)

We performed parameter sweeps of Gibbs-Thomson length scale $l_c^{Pickering}$ due to Pickering effects and the kinetic rate K. Since anterior and posterior condensates are treated differently, we consider the ratios $R^{t=360s}/R^{t=0s}$ for the two halves of the cytoplasm separately (Fig. S9C and D)

Compared to experimental observation, results in the posterior (fig. S9D) indicate that K is around 12 ($R^{t=360s}/R^{t=0s}$=1.4), which is the parameter used in Fig. 5L. Using this value of K and an anterior $R^{t=360s}/R^{t=0s}$ = 0.7, the result on the anterior side indicates that the surface tension is expected to be reduced by at least 50% (fig. S9C).

Mutant

In the *meg-3 meg-4* mutant, all effects of MEG-3 are absent, hence $l_{c,P} = l_{c,A} = 15$ nm, and the kinetic rate is reduced due to the absence of the accompanying fluidization effects. Specifically, the kinetic rate for the mutant is:

$$K_{\text{mutant},A,i} = K_{\text{mutant}} + \frac{K_{\text{mutant}}}{2} r_{A,i} \quad (14)$$

$$K_{\text{mutant},P,i} = K_{\text{mutant}} + \frac{K_{\text{mutant}}}{2} r_{P,i} \quad (15)$$

where $K_{\text{mutant}} = 2$ nm/sec, which is 6 times less than the WT value.

However, the MEX-5-induced spatially regulated phase separation remains and thus we take $c_{A,\text{out}}$ to be $1.2 \times c_{P,\text{out}}$.

The initial cytoplasmic far-field concentration is again assumed to 10% higher than c_{ss} obtained from the initial condensate size distribution.

Parameter sweeps (Mutant)

We performed parameter sweeps on the kinetic rate K. We again treat anterior and posterior condensates differently by considering the ratios $R^{t=360s}/R^{t=0s}$ separately (fig. S9E and F)

Compared to experimental observation, results on the posterior side (fig. S9F) indicate that K is around 2 ($R^{t=360s}/R^{t=0s} = 1.4$), which is the parameter used in Fig. 5M.

***C. elegans* strains**		
Strain	**Genotype**	**Reference**
EGD364	*meg-3(egx4::Halo)*	Wu et al., 2019
JH3913	*pgl-3(ax4512::Halo)*	This study
JH3914	*pgl-3(ax4320::mCherry)*	This study
JH3918	*hrde-1(tm1200);pgl-3(ax4320::mCherry)*	This study
JH3915	*pgl-3(ax4320::mCherry);meg-3(ax3055) meg-4(ax3052)*	This study
JH3919	*hrde-1(tm1200); pgl-3(ax4320::mCherry);meg-3(ax3055) meg-4(ax3052)*	This study
JH3916	*mbk-2(ax4511::Ollas);pgl-3(ax4320::mCherry)*	This study
JH3917	*mbk-2(ax4511::Ollas);pgl-3(ax4320::mCherry);meg-3(ax3055) meg-4(ax3052)*	This study
JH3920	*pgl-3(ax4320::mCherry);meg-3(ax3054) meg-4(ax3052)*	This study
JH3477	*meg-3(ax3051::Ollas) meg-4(ax3052)*	Smith et al., 2016
JH3921	*pgl-3(ax4320::mCherry);meg-3(ax4300::meGFP)*	This study

Note: *hrde-1(tm1200)* is a mutation that suppresses the RNAi insensitivity of *meg-3 meg-4* mutants (*73*).

Table S1. *C. elegans* strains.

Parameters	Values
Capillary length	15 nm
Reduced capillary length due to Pickering effects	0.15 nm
Partition coefficient	20
Cell cytoplasmic volume	30 pL

Note: Capillary length estimated as described (*57*).

Table S2. Simulation parameters.

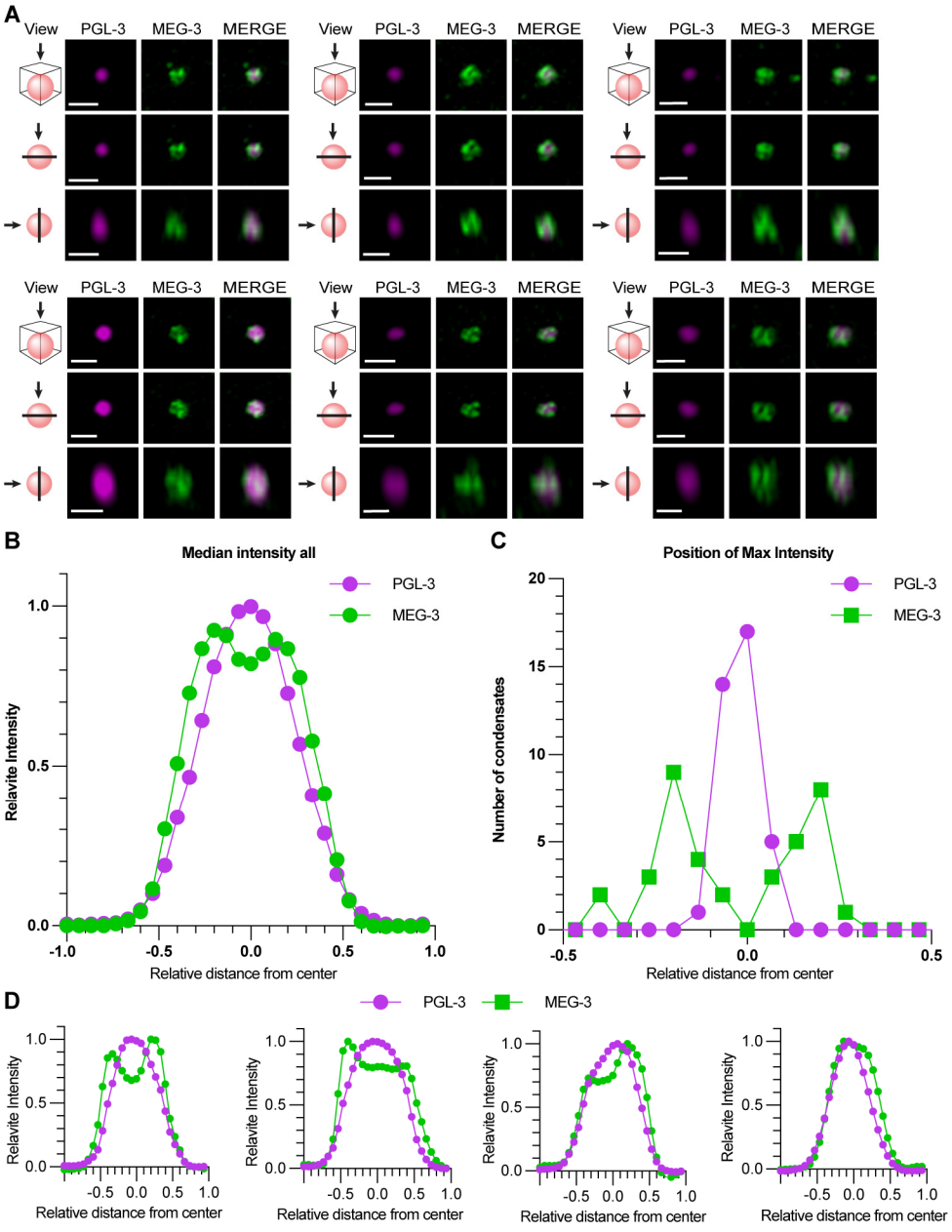

Fig. S1. MEG-3 clusters localize to the surface of PGL-3 condensates.

A) Examples of P granules labeled *in vivo* with MEG-3::meGFP and PGL-3::mCherry as in Fig. 1A. Top panels are a maximum projection of a Z-stack through the granule. Middle panels are a single X-Y plane through the middle of the same granule. Lower panels are a single Z-X plane through the middle of the same granule. Scale bars are 1 µm.

B) Graph plotting the median intensity of PGL-3 and MEG-3 fluorescence across 37 P granules imaged as in A (see Methods). MEG-3 cannot be fully resolved from PGL-3 because condensate size is near the resolution limit of the imaging used here (xy = 140 nm, z = 400 nm).

C) Graph plotting the PGL-3 or MEG-3 intensity maxima position analyzed as in B.

D) Graphs as in B showing examples of individual granules.

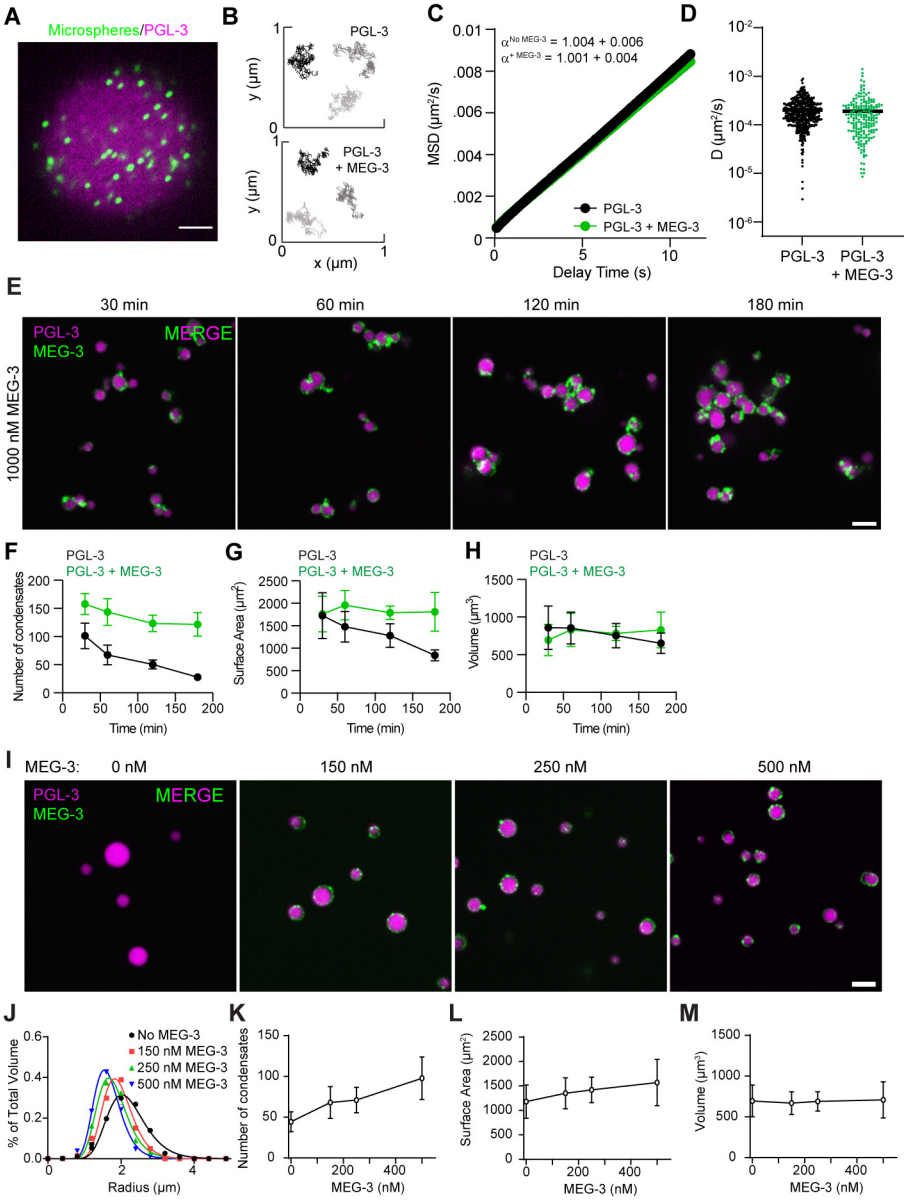

Fig. S2. MEG-3 prevents coarsening of PGL-3 condensates without changing viscosity.

A) Photomicrograph of a condensate of 3 μM PGL-3^{647} (magenta) and 80 ng/μL *nos-2* RNA with 200 nm fluorescent microspheres (green). Scale bar is 2 μm.

B) Trajectories of representative microspheres in a PGL-3 condensate assembled as in A with or without 500 nM MEG-3.

C) Mean-square displacement (MSD) versus delay time for n = 481 (No MEG-3) or n = 194 (MEG-3) tracks with length of ≥375 frames for indicated conditions. The apparent diffusive exponent (α) and diffusion coefficient (*D*) were measured by fitting MSD = $4Dt^{\alpha}$ for the first 25% of each trace.

D) Diffusion coefficients (D) calculated for microspheres in a PGL-3 condensate assembled as in (A) with or without 500 nM MEG-3.

E) Photomicrographs of PGL condensates (magenta) assembled with 3 µM PGL-3^{488}, 80 ng/µL nos-2 RNA and 1000 nM MEG-3^{647} (green) over time. Note increasing flocculation of PGL-3/MEG-3 co-condensates at 180 minutes. Scale bar is 5 µm.

F-H) Graphs depicting the number (F), total surface area (G), and total volume (H) of PGL-3^{488} in condensates at indicated time points assembled as in Fig. 12 with (green) and without (black) 500 nM MEG-3. Error bars represent SD.

I) Photomicrographs of condensates of 3 µM PGL-3^{488} (magenta) and 80 ng/µL *nos-2* RNA with indicated concentrations of MEG-3^{647} (green) after 120 min incubation. Scale bar is 5 µm.

J) Histograms of PGL condensates assembled as in I with the indicated concentrations of MEG-3. Circles indicate the fraction of volume of PGL-3 in condensates binned by the radius of each condensate. Lines indicate fit of data to a lognormal distribution.

K-M) Graphs depicting the (K) number of condensates, (L) total surface area, (M) and total volume of PGL-3 condensates assembled as in I with the indicated concentrations of MEG-3. Error bars represent SD.

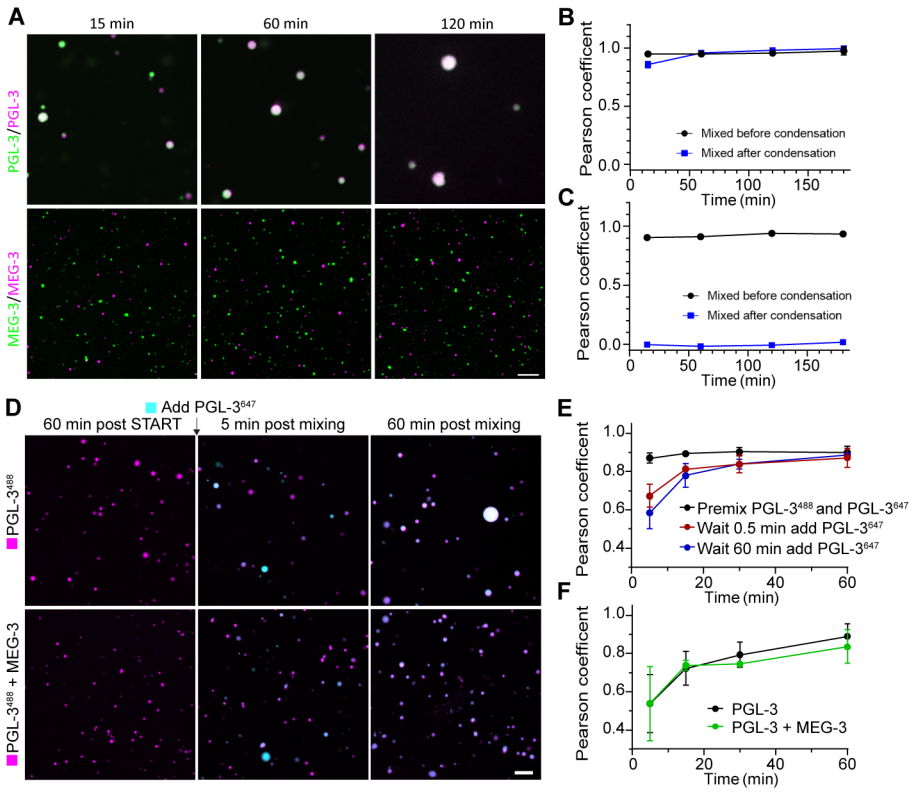

Fig. S3. PGL-3 and MEG-3 condensates have distinct exchange dynamics

A) Photomicrographs of indicated condensates at indicated timepoints after mixing. 488-labeled (green) and 647-labeled (magenta) PGL-3 (2.5 µM) or MEG-3 (500 nM + 80 ng/µL *nos-2* RNA)) protein preparations were incubated separately for 5 min before mixing (equal volumes). Scale bar is 10 µm.

B and C) Graphs showing the co-label correlation between 488-label (green) and 647-label (magenta) over time using PGL-3 (2.5 µM) (B) or MEG-3 (500 nM + 80 ng/µL *nos-2* RNA) (C). Dots represent the mean of 3 replicates and error bars are the standard deviation.

D) Photomicrographs of a PGL-3^{488} emulsion (magenta) 60 min post initial assembly and at indicated time points after addition of new PGL-3^{647} (cyan). 2.5 µM PGL-3^{488} and 80 ng/µL *nos-2* RNA were incubated for 60 min in the presence or absence of 0.5 µM MEG-3 (not shown) before adding of 2.5 µM PGL-3^{647}. Scale bar is 20 µm.

E-F) Graphs showing the co-label correlation between PGL-3^{488} and PGL-3^{647} over time. (E) PGL-3^{488} emulsions were assembled as in (D) with zero, 0.5 min or 60 min of pre-incubation before addition of new PGL-3^{647}. (F) PGL-3^{488} emulsions were assembled as in (D) with 60 min pre-incubation in the absence (black) or presence of MEG-3 (green). Each data point represents the Pearson coefficient averaged over 8 images. Error bars represent SD.

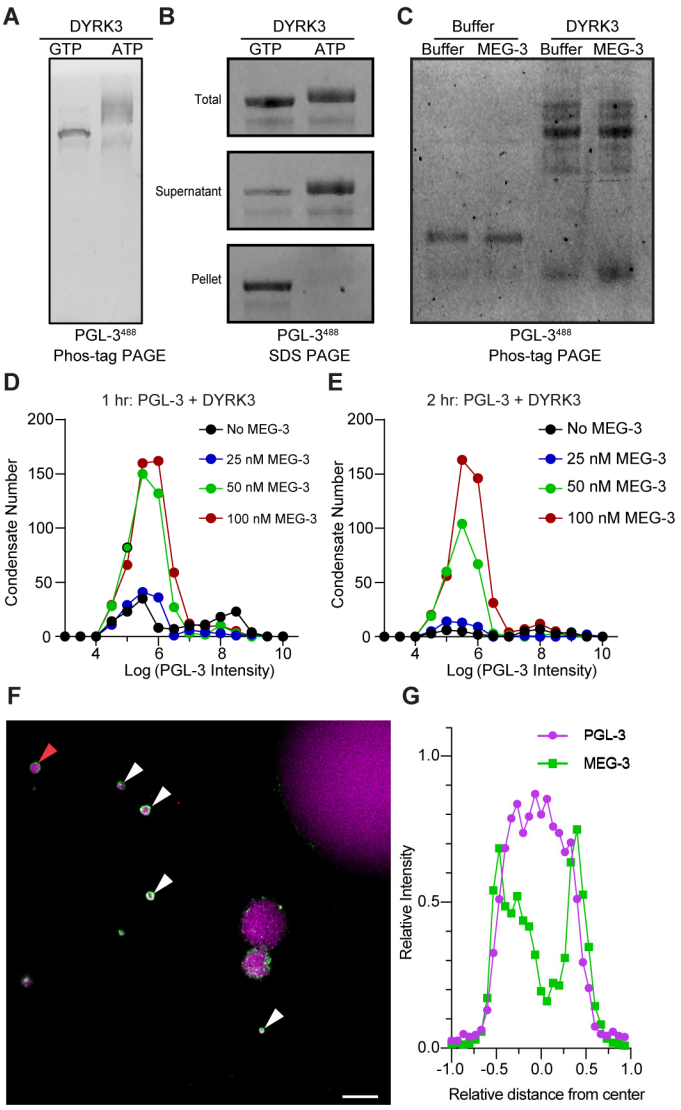

Fig. S4. DYRK-3 phosphorylates and increases the solubility of PGL-3.

A) Phos-tag SDS-PAGE of 2.5 μM PGL-3^{488} treated with 100 nM DYRK-3 kinase with 1 mM GTP or ATP. Modified PGL-3 (ATP lane) migrates more slowly than unmodified PGL-3 (GTP lane) in the Phos-tag gel. The migration of PGL-3^{488} in this gel and gels shown in B and C was visualized directly using non-confocal laser scanner.

B) 2.5 μM PGL-3^{488} treated with 100 nM DYRK3 kinase and 1 mM ATP or 1 mM GTP. Samples were spun at 12,000 rpm. The supernatant and pellet were collected, and samples were separated by SDS-PAGE.

C) 5 μM PGL-3^{488} condensates assembled with and without 100 nM MEG-3 treated with 1 mM ATP and either mock kinase buffer or 100 nM DYRK3 kinase. The reaction was stopped by addition SDS sample buffer and samples were separated by Phos-tag SDS-PAGE.

D and E) Histograms of PGL-3 condensates incubated for 60 (D) or 120 minutes (E) in the presence of 100 μM ATP, 100 nM DYRK3 and MEG-3 as indicated. Circles indicate the number of PGL-3 condensates binned by the log(Intensity) of each condensate captured from 20 images. Data shown in this

figure were obtained using the same protocol as in Fig. 3E using an independent set of experimental replicates.

F) Photomicrographs of PGL-3 condensates (max projections) assembled with and without 25 nM MEG-3 (green) and captured 60 min after addition of 100 μM ATP with and without 100 nM DYRK3. Arrows point to small PGL-3/MEG-3 condensates quantified in fig. S4G. Red arrow indicates condensate shown in Figure 3C. Scale bars is 10 μm.

G) Graph plotting the relative intensity of PGL-3 and MEG-3 fluorescence for the 5 indicated condesnates in fig. S4F (see Methods).

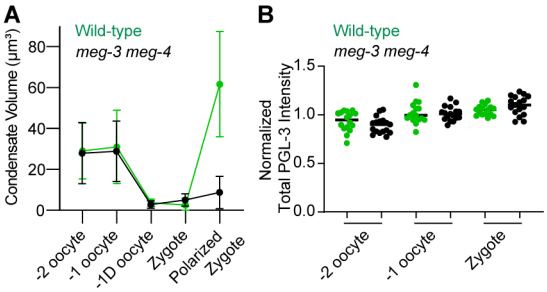

Fig. S5. MEG-3 stabilizes the PGL-3 emulsion in fertilized zygotes.

A) Graph depicting the total volume of PGL-3 in condensates in wild-type (green) and *meg-3 meg-4* mutants (black) during the oocyte-to-zygote transition at indicated developmental stages. Circles are the mean of ≥ 5 *in utero* images. Error bars represent SD. (The rapid rise in PGL-3 condensate volume in wild-type polarized zygotes is due to increased dynamics of PGL-3 condensates by MEG-3/MBK-2 – see text).

B) Graph depicting the total PGL-3 intensity in oocytes and zygotes *in utero* represented in Fig. 4A and normalized to the average intensity of each sample. Each circle represents one oocyte/zygote in wild-type (green) or *meg-3 meg-4* (black).

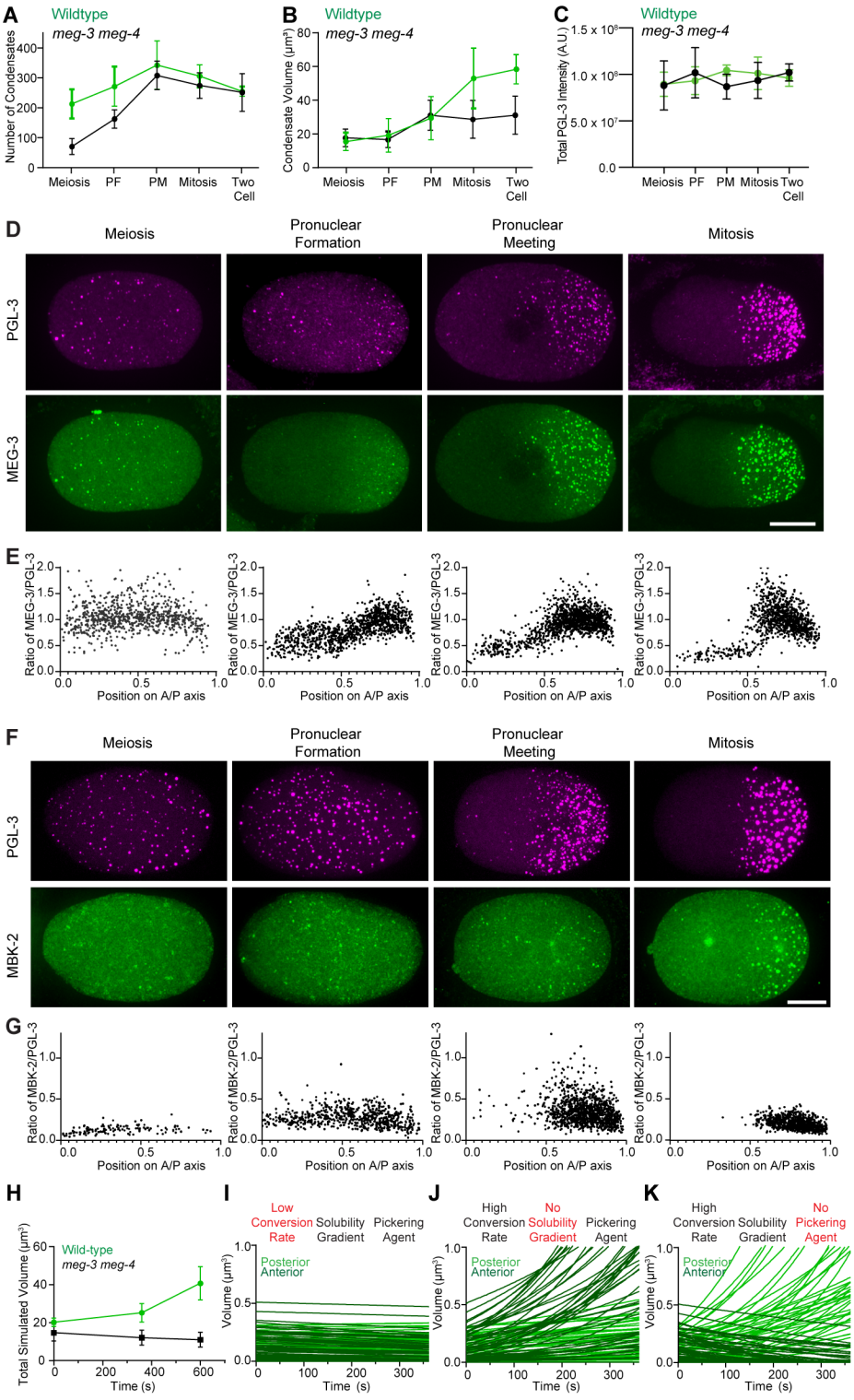

Fig. S6. PGL-3 condensate dynamics during zygote polarization.

A-B) Graphs showing the total number (A) or volume (B) of PGL-3 in condensates in wild-type (green) or *meg-3 meg-4* (black) zygotes at indicated developmental stages calculated from photomicrographs captured as in Fig. 5A. Circles represent the mean of ≥ 5 zygotes. Error bars represent SD.

C) Graph depicting the total PGL-3 intensity in zygotes represented in Fig. 5A. Each circle represents one zygote in wild-type (green) or *meg-3 meg-4* (black). Error bars represent SD.

D) Photomicrographs of zygotes expressing MEG-3::OLLAS immunostained for OLLAS and PGL-3 at indicated developmental stages. Scale bar is 10 μm.

E) Graphs depicting the ratio of MEG-3/PGL-3 relative intensity for condensates from photomicrographs captured as in (D). Each circle represents a PGL-3 condensate plotted by position in the zygote where 0 is the anterior (A) and 1 is the posterior (P).

F) Photomicrographs of zygotes expressing PGL3::mCherry and MBK2::OLLAS immunostained for OLLAS at indicated developmental stages. Scale bar is 10 μm.

G) Graphs depicting the ratio of MBK-2/PGL-3 relative intensity for condensates photomicrographs captured as in (F). Each circle represents a PGL-3 condensate plotted by position in the zygote where 0 is the anterior (A) and 1 is the posterior (P).

H) Graph showing the simulated total volume of PGL-3 in condensates representing pronuclear formation (0s), pronuclear meeting (360s), and mitosis (600s). Compare to in vivo measurements shown in panel B. Error bars represent SD.

I-K) Graphs showing the evolution of individual anterior (dark color) and posterior (light color) PGL-3 condensates under simulated experimental conditions as indicated.

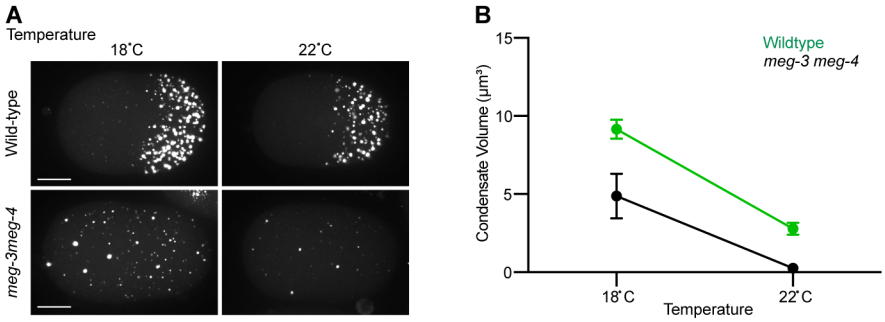

Fig. S7. Temperature-sensitivity of the PGL-3 emulsion.

A. Photomicrographs of PGL-3::mCherry condensates in live zygotes (mitosis) of indicated genotypes at 18°C and after a 4 min incubation at 22°C. Scale bar is 10 µm.

B. Graph showing average PGL-3 condensate volume in zygotes (mitosis) at 18°C and after a 4 min incubation at 22°C. Error bars represent SEM.

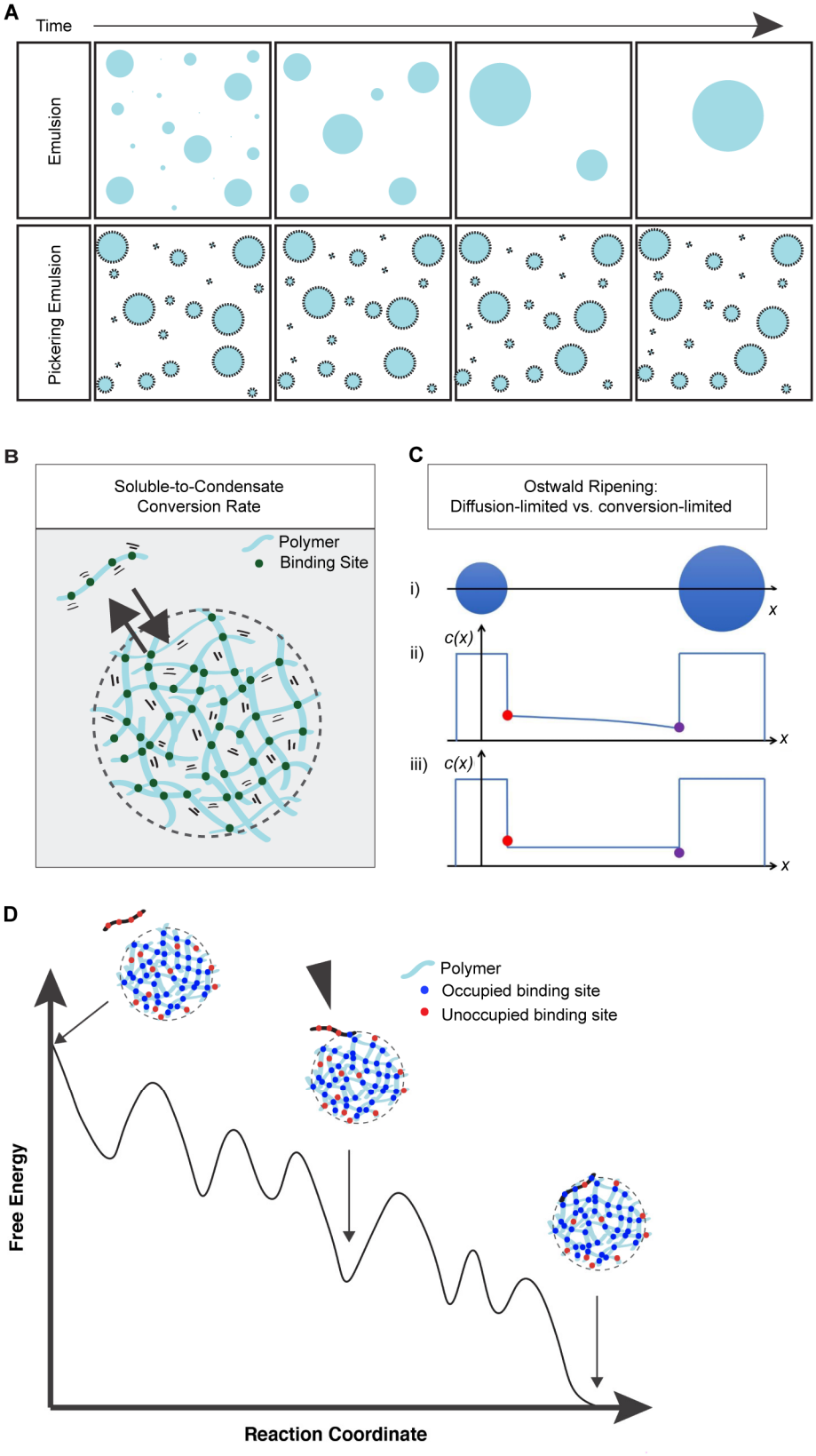

Fig. S8: Theory of condensate dynamics.

(A) Schematic depiction of an emulsion and a Pickering emulsion over time. Emulsions coarsen over time to lower free energy by reducing surface area (larger droplets have lower surface/volume ratios than smaller droplets). Pickering agents (black dots) are nanoscale solids that adsorb to the surface of condensates and reduce coarsening by lowering surface tension and interfering with coalescence (droplet fusion).

(B) Schematic depiction of a protein condensate assembled from a polymer (blue) with four binding sites (dark green). In a dynamic condensate, internal polymer rearrangement is fast and polymers in the condensate are available to bind with polymers that diffuse near the interface, leading to a high soluble-to-condensate conversion rate.

(C) Ostwald ripening: diffusion-limited scheme vs. conversion-limited scheme.

i) Consider one small and one big condensate far away from other condensates.

ii) Under the diffusion-limited scheme (the standard assumption in the Lifshitz-Slyozov theory (*68*), the concentration profile (x) along the black arrow across the condensates in i) is shown in blue. In the dilute medium, the profile is obtained by solving the diffusion equation with the boundary condition set by the solute concentration right outside the two drops. Due to the Gibbs-Thomson relation (resulting from the Laplace pressure) (*69*), the smaller condensate will have a higher solute concentration (indicted by the red dot) than that of the bigger condensate (purple dot). Due to the non-zero gradient of the diffusive profile at the drop boundaries, there is an outflux of solute from the small condensate and a corresponding influx of material into the big condensate.

iii) If the condensates are in the slow kinetic state (due to the rugged energy landscape leading to slow internal dynamics, fig. S8D), the rates of incorporation and exit of solutes into and out of the condensates can become limited compared to the time scale of concentration equilibration (due to diffusion) in the dilute medium. Therefore, the concentration profile in the dilute medium remains uniform, while the mismatches of the boundary condition at the condensates' boundaries lead to an outflux from the small condensate and an influx into the big condensate. These conditions represent a conversion-limited scheme.

(D) Schematic depiction of the free energy of one PGL-3 condensate and one neighboring PGL-3 monomer. The rugged energy landscape originates from the internal re-configuration required to accommodate the incoming PGL-3 monomer into the condensate. This reconfiguration may require several binding and unbinding events within the condensate. A similar rugged energy landscape picture has been used to explain the experimentally observed slow rate in fibril elongation (*74*).

Figure S9

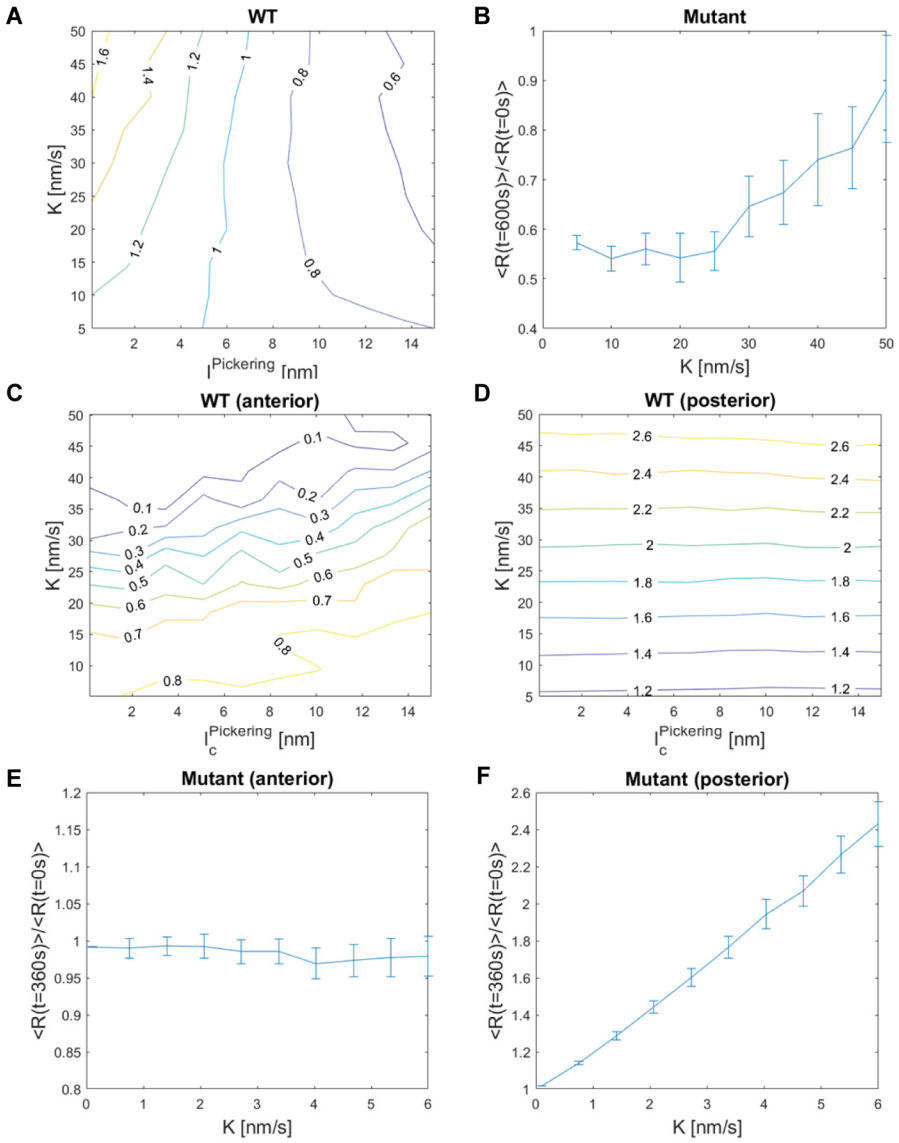

Fig. S9. Parameter sweeps of *in silico* dynamics of the PGL-3 emulsion.

A) The contour plot shows how the ratio, $R^{t=600s}/R^{t=0s}$, varies with the kinetic rate K and the Gibbs-Thomson length scale $l_c^{Pickering}$. The experimentally observed range is around 1-1.2.

B) The curve shows how the ratio, $R^{t=600s}/R^{t=0s}$, varies with K. The experimentally observed range is around 0.5-0.6. These results are obtained by averaging over 10 simulations per parameter set.

C) The contour plot shows how the anterior ratio, $R^{t=360s}/R^{t=0s}$, varies with the kinetic rate K and the Gibbs-Thomson length scale $l_c^{Pickering}$. The experimentally observed range is around 0.7.

D) The corresponding contour plot for posterior condensates. The experimentally observed range is around 1.4. These results are obtained by averaging over 50 simulations per parameter set.

E) The curve shows how the ratio, $R^{t=360s}/R^{t=0s}$, for anterior condensates varies with K. The experimentally observed range is around 1.

F) The corresponding curve for posterior condensates. The experimentally observed range is around 1.4. These results are obtained by averaging over 50 simulations per parameter set.

Movie S1.
In vivo time lapse showing PGL-3::Halo (strain JH3913). Right panel: Single molecules of PGL-3::Halo (green – JF_{646} dye sparse labeling), Left panel: PGL-3::Halo labeled P granules (magenta – JF_{549} dye heavy labeling) merged with single molecules of PGL-3::Halo (green – JF_{646} dye sparse labeling). Images are single planes at 150ms time interval, total video time is 13.45 s, playback speed is 6.67 frames per second. Scale bar is 1 μm.

Movie S2.
In vivo time lapse showing MEG-3::Halo (strain EGD364). Right panel: Single molecules of MEG-3::Halo (green – JF_{646} dye sparse labeling), Left panel: MEG-3::Halo labeled P granules (magenta – JF_{549} dye heavy labeling) merged with single molecules of MEG-3::Halo (green – JF_{646} dye sparse labeling). Images are single planes, total video time is 13 s, playback speed is 1 frames per second. Scale bar is 1 μm.

Movie S2.
In vivo time lapse showing MEG-3::Halo (strain EGD364). Right panel: Single molecules of MEG-3::Halo (green – JF_{646} dye sparse labeling), Left panel: MEG-3::Halo labeled P granules (magenta – JF_{549} dye heavy labeling) merged with single molecules of MEG-3::Halo (green – JF_{646} dye sparse labeling). Images are single planes, total video time is 13 s, playback speed is 1 frames per second. Scale bar is 1 μm.

Movie S3.
In vivo time lapse showing fluorescent microspheres diffusing within a PGL-3 condensate. Right panel: PGL-3 condensate with 80 ng/μL *nos-2* RNA (see Fig. S2A-C), Left panel: PGL-3 condensate with 80 ng/μL *nos-2* RNA and 500 nM MEG-3 (see Fig. S2A-C). Images are single planes, total video time is 180 s, playback speed is 80 frames per second. Scale bar is 1 μm.

Movie S4.
In vitro time lapse showing coalescence of PGL-3 condensates (see Fig. 2A to B). Images are single planes, total video time is 23.64 s, playback speed is 20 frames per second. Scale bar is 5 μm.

Movie S5.
In vitro time lapse showing coalescence of PGL-3 condensates (see Fig. 2A to B). Images are single planes, total video time is 49.32 s, playback speed is 20 frames per second. Scale bar is 5 μm.

Movie S6.
In vitro time lapse showing coalescence of PGL-3 condensates. Images are single planes, total video time is 174.76 s, playback speed is 20 frames per second. Scale bar is 5 μm.

Movie S7.
In vitro time lapse showing coalescence of PGL-3 condensates. Images are single planes, total video time is 135.32 s, playback speed is 20 frames per second. Scale bar is 5 μm.

Movie S8.
In vivo time lapse showing fluorescent microspheres diffusing within a PGL-3 condensate. Right panel: PGL-3 condensate (see Fig. 3D), Left panel: PGL-3 condensate with 100 nM DYRK-3 (see Fig. 3D). Images are single planes, total video time is 180 s, playback speed is 80 frames per second. Scale bar is 1 μm.

Movie S9.
In vivo time lapse of a wild-type (top panel) or *meg-3 meg-4* (bottom panel) 1 cell zygote from pronuclear formation to pronuclear meeting expressing PGL-3::mCherry (strain JH3914). Images are maximum intensity projections of Z planes spanning half of the depth of the zygote separated by 0.16 μm steps. Total video time is 428.4 s (wild-type) or 478.8s (*meg-3 meg-4*) and playback speed is 5 frames per second. Scale bars are 5 μm.

Movie S10.
In silico simulations representing 1-cell zygotes from pronuclear formation to pronuclear meeting. Each simulation includes three-model parameters: conversion rate, solubility gradient, and pickering agent. Panels represent from top to bottom 1) A wild-type zygote (see Fig. 5L). The simulation includes all three model parameters: heterogeneous high conversion rate for all condensates, higher PGL-3 solubility in anterior half of the zygote, and Pickering agent on posterior condensates. 2) A *meg-3 meg-4* zygote (see Fig. 5M). Starting condensate sizes match range observed in *meg-3 meg-4 zygotes*. Simulation includes a uniformly low conversion rate for all condensates, higher PGL-3 solubility in anterior half of the zygote, and no Pickering agent on posterior condensates. 3) A simulated zygote with a uniformly low conversion rate (see fig. S6I). 4) A simulated zygote with uniformly low PGL-3 solubility (see fig. S6J). 5) A simulated zygote lacking the Pickering agent on posterior condensates (see fig. S6K)